2012

Numerical Simulation of Wind Load on Roof Mounted Solar Panels

Yuanming Yu
University of Windsor

Recommended Citation

Yu, Yuanming, "Numerical Simulation of Wind Load on Roof Mounted Solar Panels" (2012). *Electronic Theses and Dissertations*. 218.
https://scholar.uwindsor.ca/etd/218

Numerical Simulation of Wind Load on Roof Mounted Solar Panels

by

Yuanming Yu

A Thesis

Submitted to the Faculty of Graduate Studies through the Department of Mechanical,
Automotive and Materials Engineering in Partial Fulfillment of the Requirements for the
Degree of Master of Applied Science at the University of Windsor

Windsor, Ontario, Canada

2012

Numerical Simulation of Wind Load on Roof Mounted Solar Panels

by

Yuanming Yu

Approved By:

Dr. Shaohong Cheng, External Department Reader
Department of Civil and Environmental Engineering

Dr. David Ting, Department Reader
Department of Mechanical, Automotive and Materials Engineering

Dr. Ronald Barron, Co-Advisor
Department of Mathematics and Statistics and Department of Mechanical, Automotive and Materials Engineering

Dr. Ram Balachandar, Co-Advisor
Department of Civil and Environmental Engineering and Department of Mechanical, Automotive and Materials Engineering

Dr. N. Zamani, Committee Chair
Department of Mechanical, Automotive and Materials Engineering

AUTHOR'S DECLARATION OF ORIGINALITY

I hereby certify that I am the sole author of this thesis and that no part of this thesis has been published or submitted for publication.

I certify that, to the best of my knowledge, my thesis does not infringe upon anyone's copyright nor violate any proprietary rights and that any ideas, techniques, quotations, or any other material from the work of other people included in my thesis, published or otherwise, are fully acknowledged in accordance with the standard referencing practices. Furthermore, to the extent that I have included copyrighted material that surpasses the bounds of fair dealing within the meaning of the Canada Copyright Act, I certify that I have obtained a written permission from the copyright owner(s) to include such material(s) in my thesis and have included copies of such copyright clearances to my appendix.

I declare that this is a true copy of my thesis, including any final revisions, as approved by my thesis committee and the Graduate Studies office, and that this thesis has not been submitted for a higher degree to any other University or Institution.

ACKNOWLEDGEMENTS

I would never have been able to finish my thesis without the guidance of my committee members, help from my colleagues, and supports from my family and wife.

Dr. Ting and Dr. Cheng presented a lot of interesting questions in the proposal meeting, which pushed me to think deeper and wider. Many colleagues, especially Kohei, gave me much help during my research period. I really appreciate their kind help.

I would like to take this opportunity to express my deepest gratitude to my advisors, Dr. Barron and Dr. Balachandar for their great guidance, caring, patience and providing me with an excellent research atmosphere. I also really want to thank the Natural Sciences and Engineering Research Council (NSERC) and Polar Racking Inc. for providing an NSERC Industrial Postgraduate Scholarship to carry out my research. I also offer my thanks to the University of Windsor for providing me with Graduate Assistantship opportunities during my graduate study period.

ABSTRACT

Seven RANS models (Spalart-Allmaras, k-ε, k-ω and their variants, Reynolds Stress Model (RSM)), DES-SST and LES model have been used to predict the pressure coefficient (C_p) distribution on a cube and the C_p difference of a canopy in an atmospheric boundary layer flow. The simulation results show that k-ω-SST gives the best prediction in both cases. The RSM also accurately predicts the C_p in the cube case.

The k-ω-SST and DES-SST models have been used to simulate the wind load on flat roof mounted solar panels under similar flow conditions with different wind attack angles. The simulation results demonstrate that both k-ω-SST and DES-SST give good prediction of the drag force at all wind attack angles and reasonably good prediction of the lift force at most wind attack angles. The k-ω-SST model has also been used to investigate the change of wind load on solar panels with three different configurations.

TABLE OF CONTENTS

CHAPTER 1

CHAPTER 2

CHAPTER 3

CHAPTER 4

CHAPTER 5

CHAPTER 6

APPENDIX A

APPENDIX B

LIST OF TABLES

LIST OF FIGURES

NOMENCLATURE

C_μ	Constant, used to calculate dynamic turbulent viscosity
ΔC_p	Pressure coefficient difference
C_D	Mean drag coefficient
C_L	Mean lift coefficient
h	Height of the cube or building
k	Turbulent kinetic energy
k_p	Turbulent kinetic energy at node P
l	The length scale of flow structure
p	Static pressure
p_0	Reference pressure at ambient region
p_T	Area averaged pressure at top surface
p_B	Area averaged pressure at bottom surface
T_i	Turbulent intensity
U	Velocity magnitude
U_p	Mean velocity in the near wall node P
U^*	Nondimensional velocity
u_{ref}	Reference velocity in streamwise direction
u_i	Velocity components, where *i* = 1, 2, 3 indicates x, y, z directions
u_z	Streamline velocity (x direction) at z coordinate location
u_i'	Velocity fluctuation, where *i* = 1, 2, 3 indicates x, y, z directions
x_i	Coordinates, where *i* = 1, 2, 3 indicates x, y, z directions
y^*	Nondimensional distance from wall
y_p	Distance from wall to node P

y^+	Nondimensional distance
z	z coordinate
z_{ref}	Reference height
α	Exponent of power law or wind attack angle
δ_{ij}	Kronecker delta ($\delta_{ij} = 1\ if\ i = j\ and\ \delta_{ij} = 0\ if\ i \neq j$)
τ_{ij}	Reynolds stress tensor
τ_w	Wall shear stress
ρ	Density of the fluid
μ	Dynamic viscosity of fluid
μ_t	Turbulent viscosity of the fluid
$\tilde{v}$	Modified kinematic viscosity (Spalart-Allmaras)
$\sigma_{\tilde{v}}$	Constant = 2/3 (Spalart-Allmaras)
C_{b1}	Constant = 0.1355 (Spalart-Allmaras)
C_{b2}	Constant = 0.622 (Spalart-Allmaras)
C_{v1}	Constant = 7.1 (Spalart-Allmaras)
$\mathrm{C_{w1}}$	Constant for dissipation term (Spalart-Allmaras)
f_{w}	Wall damping function, used in dissipation term (Spalart-Allmaras)
$\widetilde{\Omega}$	Component of the production term (Spalart-Allmaras)
Ω	Magnitude of the vorticity (Spalart-Allmaras)
Ω_{ij}	Rate-of-rotation tensor (Spalart-Allmaras)
f_{v1}	Viscosity damping function, used to calculate μ_t (Spalart-Allmaras)
f_{v2}	Wall damping function, used to calculate $\widetilde{\Omega}$ (Spalart-Allmaras)
δ_{ij}	Kronecker delta (Spalart-Allmaras)
κ	von Karman constant = 0.4187 (Spalart-Allmaras)

χ	Ratio of modified kinematic viscosity to viscosity (Spalart-Allmaras)
G_k	Production term of *k* equation (*k*-*ε* standard, RNG, Realizable, *k*-*ω* standard)
Y_k	Dissipation term of *k* equation (*k*-*ε* standard)
ε	Turbulent energy dissipation rate per unit mass (*k*-*ε*)
G_ε	Production term of *ε* equation (*k*-*ε* standard)
Y_ε	Dissipation term of *ε* equation (*k*-*ε* standard)
σ_k	Constant = 1.0, used in diffusion term in *k* equation (*k*-*ε* standard)
σ_ε	Constant = 1.3, used in diffusion term in *ε* equation (*k*-*ε* standard)
S	Modulus of mean rate-of-strain tensor (*k*-*ε* standard)
S_{ij}	Strain tensor (*k*-*ε* standard)
$C_{1\varepsilon}$	Constant, used in production term in *ε* equation (*k*-*ε* standard)
$C_{2\varepsilon}$	Constant, used in dissipation term in *ε* equation (*k*-*ε* standard)
α_k	Constant = 1.39, used for diffusion term in equation of *k* (RNG)
μ_{eff}	Effective viscosity (RNG)
α_ε	Constant = 1.39, used for diffusion term in equation of *ε* (RNG)
$C_{1\varepsilon}$	Constant for production term in equation of *ε* (RNG)
$C_{2\varepsilon}^*$	Constant for dissipation term in equation of *ε* (RNG)
$C_{2\varepsilon}$	Constant, used to find $C_{2\varepsilon}^*$ (RNG)
C_μ	Constant = 0.0845, used in turbulent viscosity (RNG)
η	Constant obtained from modulus of mean rate-of-strain tensor (RNG)
η_0	Constant = 4.377, used to find $C_{2\varepsilon}^*$ (RNG)
β	Constant = 0.012, used to find $C_{2\varepsilon}^*$ (RNG)
C_μ	Constant for turbulent viscosity (Realizable)
U^*	Constant, used to calculate C_μ (Realizable)

$\overline{\Omega}_{ij}$	Mean rate-of-rotation tensor (Realizable)
ω_k	Angular velocity (Realizable)
ε_{ijk}	Permutation tensor (Realizable)
A_0	Model constant = 4.04, used to find value of C_μ (Realizable)
A_s	Model variable constant, used to find value of C_μ (Realizable)
C_1	Constant, used in production term of ε equation (Realizable)
C_2	Constant = 1.9, used in dissipation term of ε equation (Realizable)
σ_k	Constant = 1.0, used in diffusion term of *k* equation, (Realizable)
σ_ε	Constant = 1.2, used in diffusion term of ε equation (Realizable)
ϕ	Constant angle, used to find A_s (Realizable)
W	Constant, related to strain tensor, used to find ϕ (Realizable)
$\tilde{S}$	Constant used to find W (Realizable)
ω	Specific dissipation rate
Γ_k	Constant of diffusion term of *k* equation (*k*-*ω* standard)
Γ_ω	Constant in diffusion term of ω equation (*k*-*ω* standard)
σ_k	Constant = 2.0, used to find Γ_k, for incompressible and high Re flow (*k*-*ω* standard)
σ_ω	Constant = 2.0, used to find Γ_ω, for incompressible and high Re flow (*k*-*ω* standard)
α^*	Constant used to find μ_t, equals 1 in high Re flow (*k*-*ω* standard)
α^*_∞	Constant used to find α^*, equals 1 for high Re flow (*k*-*ω* standard)
Re_t	Constant used to find α^* (*k*-*ω* standard)
R_k	Constant = 6.0, used to find α^* for low Re flow (*k*-*ω* standard)
α^*_0	Constant = $\frac{\beta_i}{3}$, used to find α^* for low Re flow (*k*-*ω* standard)
β_i	Constant = 0.072 (*k*-*ω* standard)

G_ω	Production term of ω equation (k-ω standard)
α	Constant used in production term of ω equation, equals 1 for high Re flow (k-ω standard)
α_∞	Constant used to find α, equals 1 for high Re flow (k-ω standard)
f_{β^*}	Constant, used to find dissipation term of k equation (k-ω standard)
x_k	Constant, used to find f_{β^*} (k-ω standard)
β^*	Constant used to find dissipation term of k equation (k-ω standard)
β^*_∞	Constant = 0.09, used to find β^* (k-ω standard)
Y_ω	Dissipation term of the ω equation term (k-ω standard)
f_β	Constant, used to find Y_ω (k-ω standard)
x_ω	Constant, used to find f_β (k-ω standard)
ζ^*	Constant=1.5 (k-ω standard)
R_ω	Constant=2.95 (k-ω standard)
F_1 , F_2	Blending functions used to find μ_t, σ_k, σ_ω (k-ω-SST)
$\tilde{G}_k$	Turbulent kinetic energy production in the k equation (k-ω-SST)
β^*	Constant = 0.09, used to find $\tilde{G}_k$ (k-ω-SST)
D_ω	Cross-diffusion modification in the equation of ω (k-ω-SST)
α_∞	Constant, used to find α (k-ω-SST)
σ_k	Constant = 1, used to find diffusion term in k equation (k-ω-SST)
$\sigma_{\omega,1}$,$\sigma_{\omega,2}$	Constants, $\sigma_{\omega,1} = 2$, $\sigma_{\omega,2} = 1.17$, used to find $\alpha_{\infty,1}$ (k-ω-SST)
$\alpha_{\infty,1}$, $\alpha_{\infty,2}$	Constants, used to find α_∞ (k-ω-SST)
$\beta_{i,1}$, $\beta_{i,2}$	Constants, $\beta_{i,1} = 0.075$, $\beta_{i,2} = 0.0828$, used to find β, $\alpha_{\infty,1}$, $\alpha_{\infty,2}$ (k-ω-SST)
C_{ij}	Convection term in stress transport equation (RSM)
P_{ij}	Production term in stress transport equation (RSM)
Ω_{ij}	Rotational term in stress transport equation (RSM)

e_{ijk}	Constant, equals 1, if i, j, k are different and in cyclic order, equals -1 in anti-cyclic order, and equals zero, if two indices are same (RSM)
D_{ij}	Diffusion term in stress transport equation (RSM)
σ_k	Constant = 0.82, used in diffusion term (RSM)
Φ_{ij}	Pressure strain term in stress transport equation (RSM)
$\phi_{ij,1}$	Low pressure strain term in equation of Φ_{ij} (RSM)
$\phi_{ij,2}$	Rapid pressure strain term in equation of Φ_{ij} (RSM)
$\phi_{ij,w}$	Wall reflection term in equation of Φ_{ij} (RSM)
C_1	Constant = 1.8, used to find $\phi_{ij,1}$ (RSM)
C_2	Constant = 0.6, used to find $\phi_{ij,2}$ (RSM)
C_1' , C_2'	Constants, C_1' = 0.5, C_2' = 0.3, used to find $\phi_{ij,w}$ (RSM)
C_s	Smagorinsky constant (LES)
F_{DES}	Constant, used in dissipation term of k equation (DES-SST)
C_{des}	Constant = 0.61, used to find F_{DES} (DES-SST)
L_t	Turbulent length scale, used to find F_{DES} (DES-SST)

CHAPTER 1

Introduction

1.1 Methods to Determine Wind Loads on Solar Panels

One of the factors that affect application of solar photovoltaic cells is how to accurately estimate their survivability and performance under wind loading. Currently, there are two ways to estimate the wind load on a solar panel. One way is to use tables provided by the industry codes such as ASCE 07-05 (American Society of Civil Engineering). However, since these tables in the code are not explicitly intended for roof-mounted solar panels, their application may produce different results from different structural engineers. The second way to estimate the wind load on a solar panel is wind tunnel testing. Through wind tunnel tests on a solar panel in one wind flow direction (such as North, which is usually defined as 0^o), the peak wind load in that direction is determined. Then, for a symmetric building, the process is repeated in increments of 10^o, from 0^o to 180^o, finding the peak load in each direction. The maximum wind load among them is selected and multiplied by a safety factor to produce the final wind load. The final wind load is used as the design wind load on solar panels.

With the advancement of computer hardware technology and the development of the Computational Fluid Dynamic (CFD) methodology, numerical simulation of the wind aerodynamics of solar panels is destined to become a third approach to find the wind load on roof-mounted solar panels.

1.2 Flow around a Cubic Shaped Building

When wind approaches a low-rise building from the normal direction, the flow separates at both the leading edge of the roof and the side wall front edge, creating very unstable shear layers. These shear layers separate the flow inside the separation zone from the outside free stream flow. Subsequently, these shear layers may reattach on the roof and side wall, or may not, depending on the depth of the building. Several kinds of vortex structures develop around the building. On the top, the separation of the top shear layer creates a bound recirculation, a 'top vortex', which is located on the roof near the leading edge. This top vortex creates a high negative pressure zone on the roof. At the front of the building, near the base of the windward wall, a horseshoe vortex is generated due to the roughness of the floor and presence of the obstacle. Along both sides, a side vortex occurs due to the flow separation at the sidewall leading edge, which originates from the channel floor. At the back of the cube, an arch-shaped vortex develops, which is confined by the side flow, top flow and leeward wall. When the wind is at an oblique angle, a conic vortex develops due to the presence of the two roof edges. These highly unstable vortices create the highest negative pressure on the roof [18]. Due to the existence of a pressure gradient and roughness of the upstream terrain, winds are usually gusty and unsteady. The peak pressure on the surface of a building created by gusty winds has an important role on wind loading on the building, and the magnitude of the peak pressure may be much higher than the mean value of the pressure [11].

1.3 Previous Predictions of Pressure Distribution on a Cube Building

Shuzo [31] has simulated natural boundary layer flow over a cube using the k-ε turbulence model [14] with different boundary conditions and levels of mesh fineness. He found that the turbulent kinetic energy in the separation region is over-estimated. Richards [25] has reviewed the problem of flow around a cube in the Computational Wind Engineering 2000 Conference Competition. Reynolds Averaged Navier-Stokes (RANS) models, in particular k-ε standard, k-ε RNG [39] and k-ε MMK [34] were implemented. On the windward and leeward face, both horizontal and vertical centreline pressure match well with full scale data. However, on the roof, the numerical results deviate significantly from full scale data. On the side face, the k-ε RNG performs better than the other two models. The velocity field prediction is noticeably better than the pressure prediction. Köse and Dick [12] used RANS models (k-ε standard, k-ω SST [20]) to predict the pressure coefficient distribution around a 6 m high building and compared their results with experimental data. At both the windward face and leeward face on the symmetry plane, the RANS models gave good prediction in pressure. However, at the roof, the difference between numerical simulation and measurement is large. The prediction of velocity field is reasonably good, except in the wake region.

Using Large Eddy Simulation (LES) of bluff body flow, Shah and Ferziger [29] simulated fully developed channel flow around a cube, based on the experiments of Martinuzzi and Tropea [18]. The mean velocity distribution contour at the symmetry plane has good agreement with the experiment result. The time-averaged streamwise turbulence also has a good match with experimental data. Unfortunately, no pressure coefficient distribution was presented. Nozawa and Tamura [23] predicted the mean, root-mean-square (RMS) and peak pressure coefficient distribution on a low-rise building under natural boundary layer flow using LES with dynamic version [7] of the Smagorinsky-Lilly subgrid model [15]. The Reynolds number based on building height and upstream velocity at building height was $2 x 10^4$ and the inlet fluctuation was introduced from a separate LES simulation, based on the technique proposed by Lund et al. [17]. Compared with experimental data, the mean pressure coefficient showed good accuracy, the RMS value had a reasonable match except on the roof area near the leading edge, and the peak value was within the range of full scale measurement.

Köse and Dick [12] used a Detached Eddy Simulation (DES) model with RANS model of k-ω-SST [20] to predict flow over a cube at Reynolds number of $4 x 10^4$ and $4 x 10^6$. At the lower Reynolds number, DES could predict the velocity field very accurately. Unfortunately, there was no pressure coefficient comparison between DES and experimental data. At the higher Reynolds number, $4 x 10^6$, the DES model failed to predict the pressure coefficient on the roof. Haupt et al. [10] used DES with the Spalart-Allmarar (SA) option [33] and zonal DES [16] to simulate atmospheric boundary layer flow over a cube with Reynolds number of $4 x 10^6$. Both DES and zonal DES have the capability to predict the pressure coefficient at the windward face and leeward face. However, the pressure coefficient on the roof is not so good, although zonal DES gives much better prediction than DES.

1.4 Prediction of Wind Load on a Roof Mounted Solar Panel by Wind Tunnel Test

Adrian [1,2] conducted wind tunnel tests on solar panel arrays installed on the roof of a five-story building model. He found that a parapet greatly reduced the wind speed on surface of the solar panels, while the turbulence intensity remains the same. The difference between the measure of pressure with pneumatic average and calculated mean pressure is negligible. The sheltering effect of the first row of solar panels and the building itself on the second row of panels is significant. Graeme et al. [9] conducted a parametrical study of the wind load change on flushed mounted solar panels on a flat roof with the change of solar panel height and lateral distance. He found the change of vertical distance from the solar panel to the roof (from 6 mm to 14 mm with scale of 100) and the lateral distance between each panel (4 mm to 8 mm with the scale of 100) have only a minor effect on the wind load, except at the roof leading edge.

1.5 Prediction of Wind Load on a Roof Mounted Solar Panel by CFD

Bronkhorst et al. [5] conducted three-dimensional CFD simulations with the k-ε RNG model and the Reynolds Stress Model (RSM) [13]. The solar panel model was made in a solid block with scale of 1:50 and tilt angle of 35^{o}. The building is 30 m in breadth, 40 m in depth and 10 m in height. A structured mesh was used in the simulation and, at the computational domain inlet, atmospheric boundary layer velocity and turbulent intensity profiles were implemented. After comparison with wind tunnel test results, the authors found that the median pressure coefficient predicted by k-ε RNG had 39% difference with the experiments, while the Reynolds Stress Model had a difference of 35%. In the wake of the solar panel row, the agreement was even worse due to the incorrect prediction of the separation zone. Zhou and Zhang [40] conducted a three-dimensional CFD simulation using finite element software, ADINA, to investigate the difference between wind loads on a roof with and without solar panels installed. They found that the wind load increased significantly due to installation of the solar panels.

1.6 Conclusions

RANS models (k-ε RNG and k-ω-SST) and DES with a shear stress transport (SST) or Spalart-Allmaras (SA) option can predict the pressure distribution at the windward face and leeward face. However, the prediction on the roof is problematic. LES can accurately predict the pressure distribution on the roof and it provides reasonable results for the RMS value only when the Reynolds number is low. RANS models (k-ε RNG and RSM) do not provide an accurate pressure distribution on roof-mounted solar panels.

1.7 Objectives of the Thesis

Based on a search of the literature, it appears that there are no studies on LES and DES simulations of the wind load on roof-mounted solar panels, and no CFD simulations on wind load prediction with a fully unstructured mesh. In the current thesis, due to complexity of the geometry of solar panel arrays, a fully unstructured mesh will be applied and investigated. Two validation cases and one industrially sponsored project will be simulated. The two validation cases will be simulated using most of the well-known RANS models, a DES model and an LES model. For the industrial project the k-ω-SST model, which shows the best performance, and DES will be used to predict the wind load. Finally, the wind loading on three solar panel configurations will be predicted by the k-ω-SST model. These three configurations account for i) an increase in lateral distance (gap) between solar panels from 0 to 2.5 inches, ii) elevation of the solar panel array by 6 inches off the roof, and iii) elevation of the solar panel array to the same level of a 2.5 foot installed parapet.

The first validation case concerns using RANS models, DES and LES to predict the pressure coefficient distribution on a cube in an atmospheric boundary layer flow. Results are compared with wind tunnel tests [31]. The second validation case uses these same models to predict the mean wind load and peak wind load on a canopy under similar flow conditions as the cube. The results from these simulations are compared with experimental data of Ginger and Letchford [8]. The calculated peak force from the LES and DES simulation results is based on the method of covariance integration [8].

CHAPTER 2

Pressure Coefficient on a Cube in an Atmospheric Boundary Layer

2.1 Flow Problem Description

Shuzo [31] performed both wind tunnel tests and numerical simulations on the flow over a cube with 200mm length. In numerical simulations of flow over surface-mounted objects, it is important to ensure that the approaching flow accurately represents the physical situation. The experimental results of Shuzo [31] and the simulation results from the current study for the upstream velocity profile and turbulent intensity profile are shown in Figures 2-1a and 2-1b, respectively. These figures show the velocity and turbulent kinetic energy at the cube location, but without presence of the cube. In these figures, h is cube height and u_{ref} is the velocity at cube height at the location of the cube. The non-uniform unstructured mesh used in these calculations is able to accurately capture the velocity all the way to the bed. However, there is noticeable disagreement between the numerical simulation and wind tunnel data near the bed for the turbulent kinetic energy. This is likely due to inaccuracies in both the experimental and numerical methodologies, because of difficulties with near-bed measurements of turbulence and the coarse mesh near the bed used in the simulation.

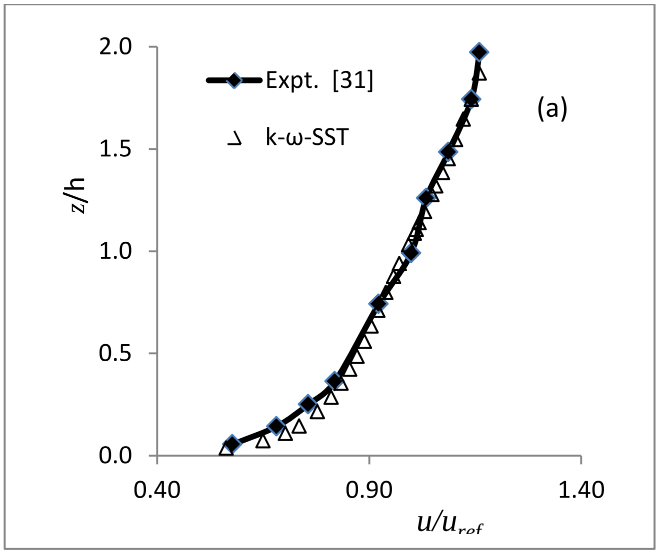

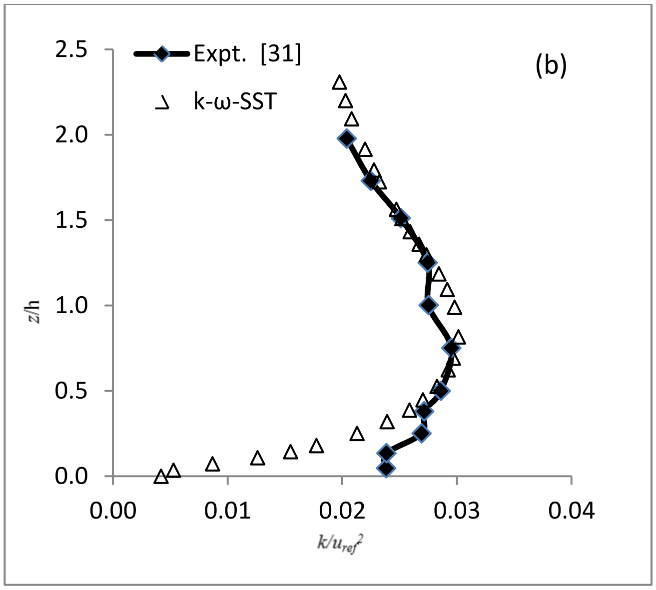

Fig. 2-1 Comparison of experimental results and numerical prediction (k-ω-SST) at cube location, without presence of the cube, (a) velocity profile; (b) turbulent kinetic energy

2.2 Governing Equations

The equations that govern the unsteady flow of an incompressible fluid are [35]

$$\frac{\partial u_i}{\partial x_i} = 0 \qquad (2\text{-}1)$$

$$\rho \frac{\partial u_i}{\partial t} + \rho \frac{\partial (u_j u_i)}{\partial x_j} = -\frac{\partial p}{\partial x_i} + \frac{\partial}{\partial x_i}(\mu \frac{\partial u_i}{\partial x_j}) \qquad (2\text{-}2)$$

where u_i, p, ρ and μ denote the velocity components in the Cartesian coordinate system x_i, (i = 1, 2, 3), pressure, density and dynamic viscosity, respectively. Equations (2-1) and (2-2) are the well-known Navier-Stokes (N-S) equations.

There are three ways to treat these equations for turbulent flows. One method, which forms the basis for Reynolds Averaged Navier-Stokes Equations (RANS), is to perform time-averaging. The second method uses a spatial filtering operation, which is the methodology used for Large Eddy Simulation (LES). The third method is Direct

Numerical Simulation (DNS). DNS is extremely computationally expensive and is not considered in this thesis.

2.2.1 Reynolds Averaged Navier-Stokes (RANS)

If the N-S equations are time-averaged, second-order moment terms, which represent the fluctuation of Reynolds stress, will arise in the equations. This procedure adds six new unknowns, the Reynolds stresses, to the set of four equations above. Turbulence models have been developed to close the time-averaged N-S equations. There are models based on one equation, e.g., Spalart-Allmaras [32] (see eqn. (A-2) in Appendix A), and two equations, e.g., k-ε standard developed by Launder and Spalding [14] (see eqns. (A-3), (A-4)); RNG, renormalization group devise by Yakhot et al. [39] (see eqns. (A-5), (A-6)); Realizable, proposed by Shih et al. [30] (see eqns. (A-3), (A-7)); k-ω, proposed by Wilcox [37] (see eqns. (A-8), (A-9)); k-ω-SST, devised by Menter [20] (see eqns. (A-10), (A-11)). The Reynolds stresses are calculated based on the assumption that there exists an analogy between the action of viscous stresses and Reynolds stresses on the mean flow, which is referred to as the Boussinesq assumption (see eqn. (A-1)).

Both one equation and two equation models are referred to as turbulent viscosity models and are based on the assumption that the turbulent viscosity is isotropic in space. This assumption is not valid in many flow situations. To overcome this deficiency the Reynolds Stress Model (RSM) (also called Differential Stress Model) proposed by Launder et al. [13], has been developed (see eqn. (A-12)). This model uses a stress transport equation for each component of the Reynolds stress tensor to solve the anisotropic problem of the flow.

2.2.2 Large Eddy Simulation (LES)

The second method to close the N-S equations is to conduct a spatial filtering operation on the N-S equation. Eddies larger than the filter space will be calculated while the smaller eddies will be simulated by a subgrid-scale model. The characteristics of large eddies are more problem dependent, which are primarily determined by the geometry of the flow, while small eddies are more isotropic, and are suitable for modeling. This is the essence of large eddy simulation (LES). LES falls between DNS and RANS in terms of the fraction of the resolved scales. Though in theory it is possible to resolve the whole spectrum of the turbulence scales using DNS, in the current stage of development, it is impossible to conduct DNS for practical industrial use.

The Smagorinsky subgrid-scale (SGS) model, based on assumption of the Boussinesq hypothesis, has been used in current research. The subgrid stresses are calculated by equation (A-13).

The dynamic SGS model proposed by Germano et al. [7] is used to determine the SGS stresses with two different filtering operations, with cutoff widths Δ_1 and Δ_2 (see eqn. (A-14)). Since, in the case of bluff body flow problems this option usually gives better simulation results [22], it is used in the current work.

Large Eddy Simulation (LES) need much more computing power than RANS models, but it gives more accurate results than the RANS model in the case of bluff body flow [22].

2.2.3 Detached Eddy Simulation (DES)

In the Detached Eddy Simulation (DES) approach, the unsteady RANS models are employed in the boundary layer and the LES models is applied in the separated regions. DES models have been specially designed to address high Reynolds number wall-bounded flows, where the cost of computation is very high when using LES over the entire flow field. The computational cost for DES is lower than LES but is higher than RANS.

Fluent offers three types of RANS model for DES, the Spalart-Allmaras model, the *k*-*ε* Realizable model and the *k*-*ω*-SST model. In the current research, *k*-*ω*-SST based DES proposed by Menter et al. [20] will be used. The reason for choosing this model is that the *k*-*ω*-SST model demonstrates relatively better prediction in the two validation cases.

2.3 Near-Wall Treatment

Traditionally, there are two approaches to model the near-wall flow region. One approach is to use the “standard wall function”, which uses an empirical equation to “bridge” the viscous layer to the outer layer, and the viscous region is not resolved [3]. Another approach is to use a wall model near the wall [3], so the flow inside the three layers all get resolved. The mesh near the viscous layer usually is very fine. Details of these models can be found in Appendix B.

2.4 Computational Domain and Test Cases

Setting the size of the computational domain is not an easy or straightforward task. Choosing the computational domain too large will waste computational resources and time, while picking too small of a computational domain will give inaccurate solutions. Three domain sizes are listed in Table 2-1. Domain II is recommended in the Best CFD Performance Guide [6], domain I was reported by Köse and Dick [12] to give similar simulation results as those from a much larger domain size, and domain III is considered here to see whether this large domain will improve the simulation results. These three domain sizes are used for the initial simulation with one of the RANS model, *k*-*ω*-SST, which is selected due to the accuracy in the C_p prediction, to be demonstrated below. Figures 2-2 and 2-3 show domain II layout in the horizontal plane and cross-section, together with the boundary conditions imposed on the flow. From these initial tests with the *k*-*ω*-SST model, after comparison with experimental data, it was determined that domain II is the most suitable and therefore will be used for further simulations. The simulation results of C_p on the symmetry plane of the cube are shown in Fig. 2-4.

Table 2.1 Extent of computational domain (h: cube height)

Domain	# of cells	Upstream length	Downstream length	Lateral	Vertical
I	220,000	3h	10h	3h	3h
II	400,000	5h	20h	5h	5h
III	850,000	5h	30h	10h	10h

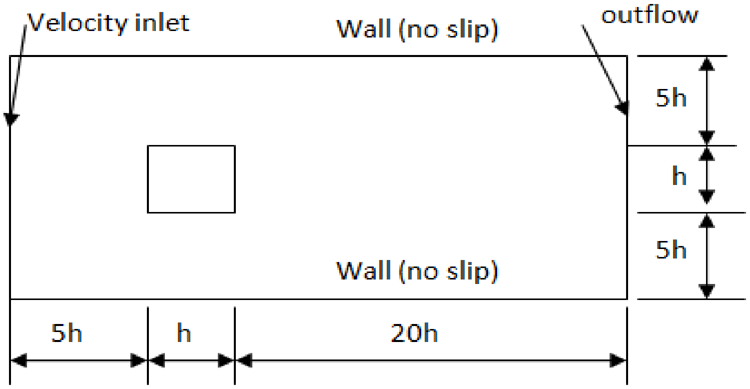

Fig. 2-2 Computational domain II (horizontal layout, not to scale)

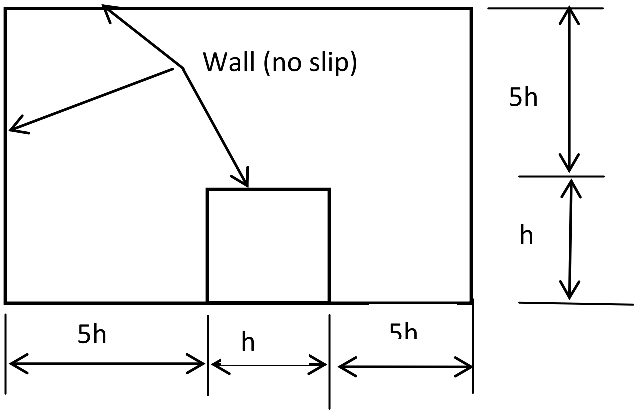

Fig. 2-3 Computational domain II (cross-sectional layout, not to scale)

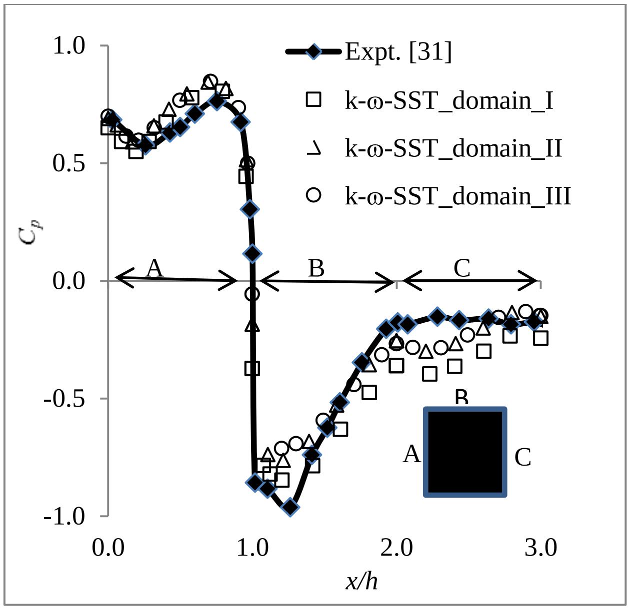

Fig.2-4 Effect of computational domain size on C_p distribution

2.5 Boundary Conditions

The velocity at the inlet is taken as

$$u_z = u_{ref}(\frac{z}{z_{ref}})^{\alpha} \tag{2-3}$$

where u_z , u_{ref}, z_{ref}, z, α are streamwise velocity component, reference velocity, reference height, elevation and exponent, respectively. The turbulent kinetic energy and dissipation rate are determined from

$$k = \frac{3}{2}(u_{ref}T_{i)}{}^{2} \tag{2-4}$$

$$\varepsilon = C_{\mu}^{3/4}\frac{k^{3/2}}{l} \tag{2-5}$$

where C_μ is a constant and T_i is the turbulence intensity, as recommended in the literature [35]. The definition of specific dissipation rate and viscosity ratio are given by

$$\omega = \frac{\varepsilon}{kC_{\mu}} \tag{2-6}$$

$$\frac{\mu_t}{\mu} = \frac{\rho}{\mu} C_\mu \frac{k^2}{\varepsilon} \qquad (2\text{-}7)$$

For DES and LES, the inlet turbulence is generated using the vortex method [19]. The downstream exit is specified as an outflow. The top surface, side surfaces, bottom surface and cube surface are all considered as no-slip walls.

For k-ε standard, k-ε RNG, k-ε Realizable and Reynolds Stress Model, scalable wall function [3] is used to avoid deterioration of the standard wall function when the mesh cells gets too fine.

For LES, the Werner-Wengle wall function [36] is used to alleviate the strict fine mesh requirement near the wall for high Reynolds number wall-bounded flows.

2.6 Mesh Topology

A tetrahedral mesh has been constructed to discretize the computational domain, using Gambit 2.4. A tetrahedral mesh is not commonly used in the wind engineering literature due to its lower efficiency of discretization of space compared with a structured mesh. But it has the important advantage of flexibility. In this work a non-uniform unstructured mesh has been used with a finer mesh implemented in regions of high gradients. The mesh layout in the vertical symmetry plane for the present simulations is illustrated in Fig. 2-5. There are approximately 25 cells along each edge, with the total number of cells reaching about 400,000.

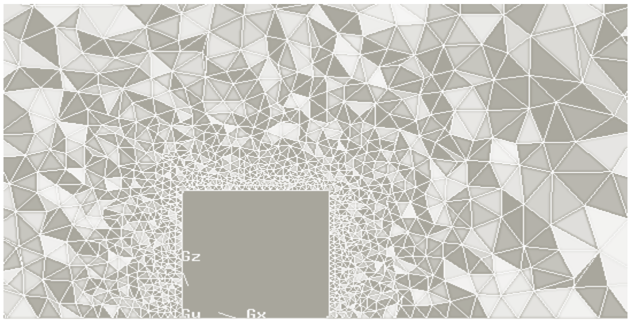

Fig. 2-5 Tetrahedral mesh around the cube

2.7 Numerical Setup

For most of the RANS models (except RSM), third-order accuracy is used for spatial discretization of the convection terms in both the momentum equations and turbulence equations, while second-order accuracy is used for the pressure interpolation. The solution algorithm uses pressure based, pressure-velocity coupling. For RSM, the second-order upwind scheme is used for convection terms, while the solution algorithm uses pressure based, segregated, SIMPLE [24]. For the LES and DES simulations, bounded central differencing is used for momentum equations. The time discretization is implicit second-order. The Courant-Friedrichs-Lewy number is around 5 for LES and around 10 for DES. The drag coefficient and a continuity equation residual less than 10^{-7} have been used as the converge criteria.

2.8 Simulation Results

2.8.1 C_p Distribution in Vertical Symmetry Plane of the Cube

The pressure coefficient, C_p, is defined as

$$C_p = \frac{(p-p_0)}{\frac{1}{2}\rho u_{ref}^2} \tag{2-8}$$

where p and p_0 are static pressure and reference pressure, respectively. The simulation results from each of the turbulence models are compared with experimental data of [31] in Figs. 2-6, and 2-7.

a). Windward symmetry plane

The k-ω-SST model shows the best performance for the prediction of C_p on the front of the cube, closely matching with experimental data as seen in Fig. 2-6a. The Reynolds Stress Model ranks second, as illustrated in Fig. 2-6b. Although it could not predict the C_p increase near the ground level, which is due to the effect of front wall recirculation, for most of the front face, RSM yields a good overall prediction. The least accurate prediction is the k-ω standard result which, as shown in Fig. 2-6a, over-predicts C_p by four-fold. The second worst performance is k-ε standard (Fig. 2-7a), over-predicting C_p by a factor of two. In fact, these models predict a C_p value much great than 1. The reason for this will be discussed in section 2.8.2. The Spalart-Allmaras model (Fig. 2-6b), *k*-*ε* RNG and *k*-*ε* Realizable (Fig. 2-7a) have similar performance., all of them predict the correct shape of the C_p curve only slightly over-predict the C_p near the leading edge region. Both DES-SST and LES (Fig. 2-7b) accurately predict C_p on the windward face, although LES appears slightly closer to the experimental data.

b). Roof symmetry plane

Considering only the roof portion of the cube, RSM has the best prediction of C_p, closely matching the experimental data (Fig. 2-6b); *k*-*ω*-SST and *k*-*ε* RNG also both give good prediction on the roof. The *k*-*ϖ*-SST model slightly under-predicts the suction pressure near the leading edge, while *k*-*ε* RNG slightly over-predicts the suction pressure. The SA model over-predicts the suction pressure near the leading edge and under-predicts it over the main region. The *k*-*ω* standard, *k*-*ε* standard and *k*-*ε* Realizable fail to predict the C_p on the roof; they significantly over-predict the suction pressure on the leading edge and under-predict the suction pressure in the remaining region. Both DES-SST and LES slightly over-predict the suction pressure on the roof, but still are in an acceptable range. DES-SST results appear to be closer to the experimental data than LES.

c). Leeward symmetry plane

On the leeward side, the experimental C_p shows constant negative value (around -0.2) from the top of the cube to ground level in the symmetry plane, while all the RANS models show only a slight deviation from this constant value. In general, all the RANS models not only have similar performance but also are very close to the experimental data. Both DES and LES significantly over-predict the suction pressure along the leeward wall.

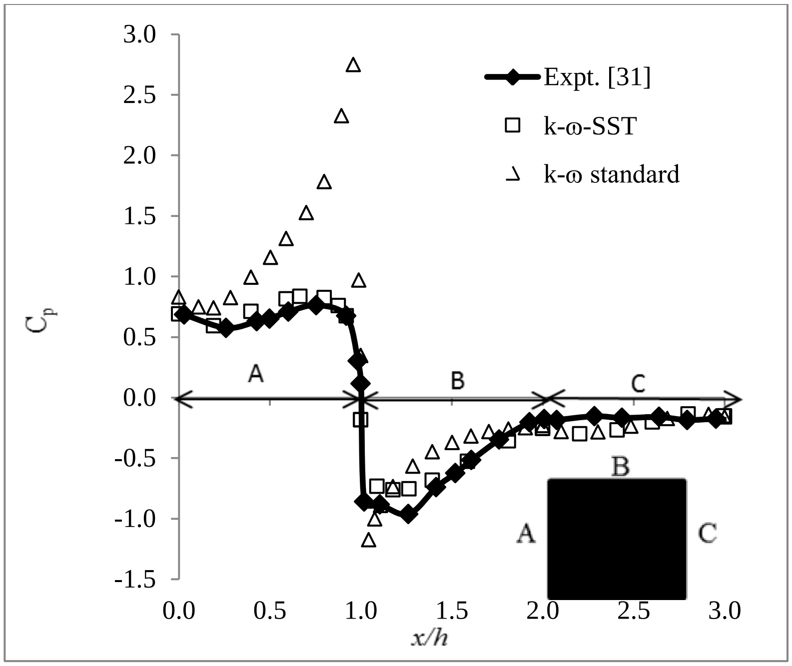

(a)

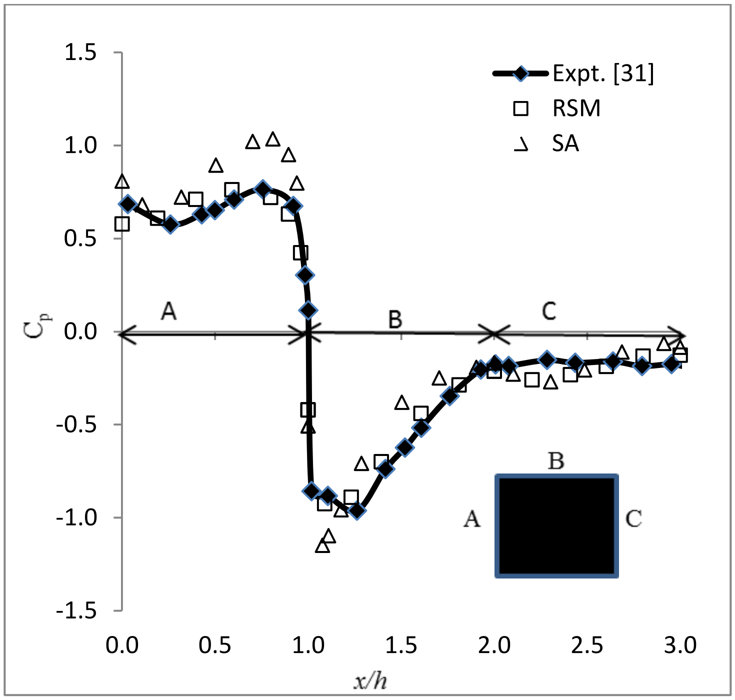

(b)

Fig. 2-6 C_p distribution at vertical symmetry plane from (a) *k-ω* standard and *k-ω*-SST models; (b) Reynolds Stress Model (RSM) and Spalart-Allmaras (SA) model

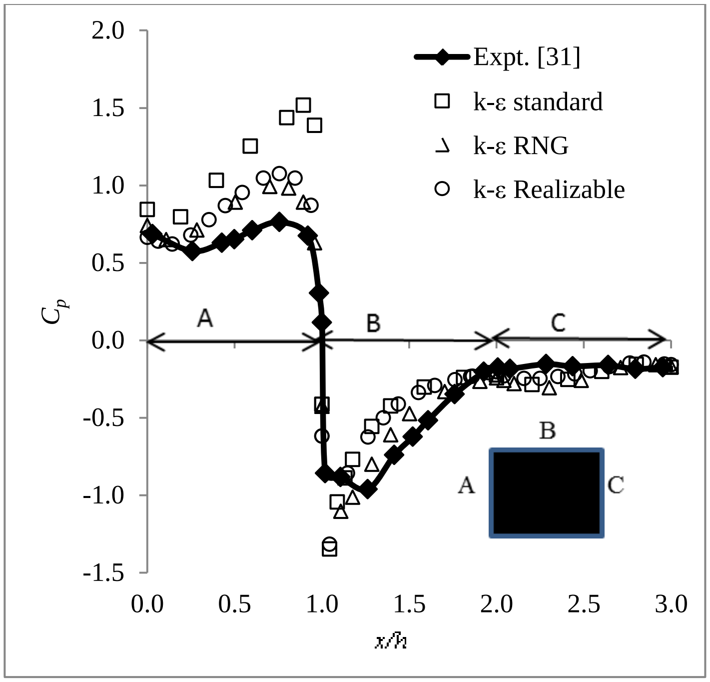

(a)

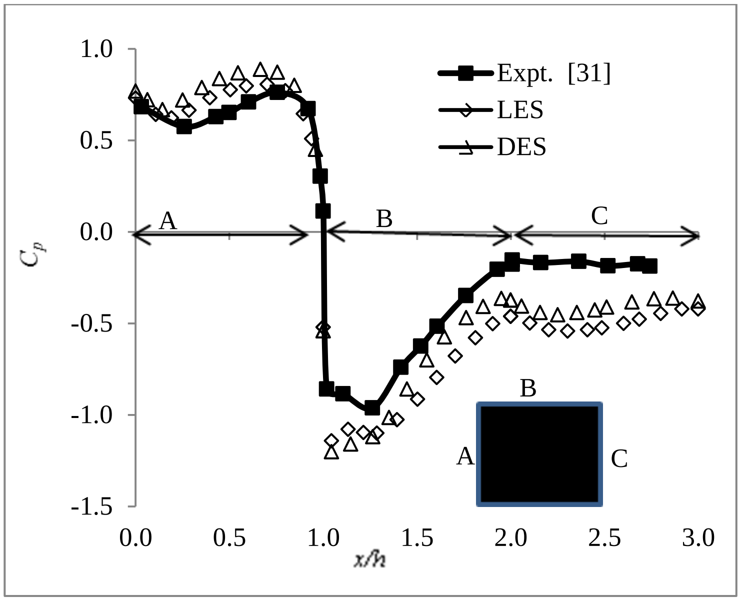

(b)

Fig. 2-7 C_p distribution at vertical symmetry plane from (a) *k*-*ε* standard, *k*-*ε* RNG and *k*-*ε* Realizable models; (b) DES–SST and LES (dynamic Smagorinsky) models

2.8.2 Flow Pattern around the Cube

The streamtraces pattern near the cube in the vertical symmetry plane and a horizontal plane near the ground, predicted by the seven RANS models, DES-SST and LES, are presented in Figs. 2-8 to 2-16. Most models have predicted the ring vortex, roof separation bubble, side separation and wake recirculation, but the shapes and locations are different from each other. As seen in Fig. 2-9a and Fig. 2-12a, both k-ε standard and k-ω standard fail to predict the roof separation. This is the reason that the predicted C_p from these models rises to a value greater than 1. The flow patterns from RANS models are more symmetrical than those from DES-SST and LES. The reason for this may be that the simulation times for the DES-SST and LES are not long enough. Since there is no experimental information about the streamtraces pattern, one should be cautious to speculate which model predicts the more realistic flow pattern. Nevertheless, based on the C_p discussions above, it appears that the k-ω-SST provides the most reliable results over the entire cube.

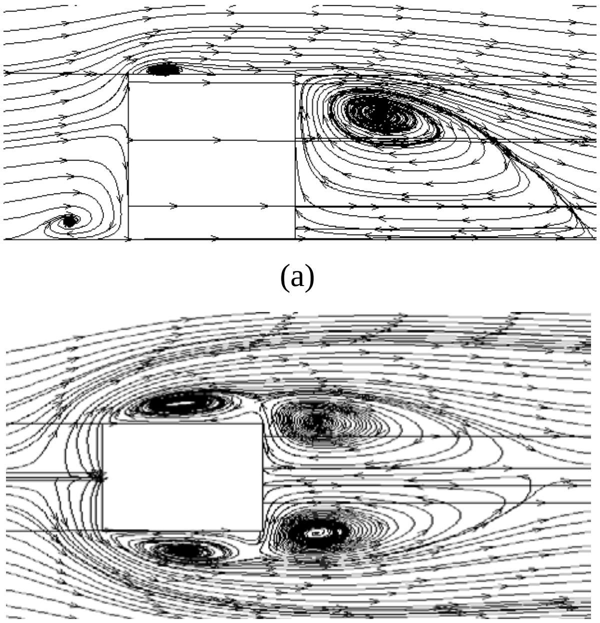

(a)

(b)

Fig. 2-8 Streamtraces predicted by Spalart-Allmaras model, (a) vertical symmetry plane; (b) horizontal plane at 0.125h

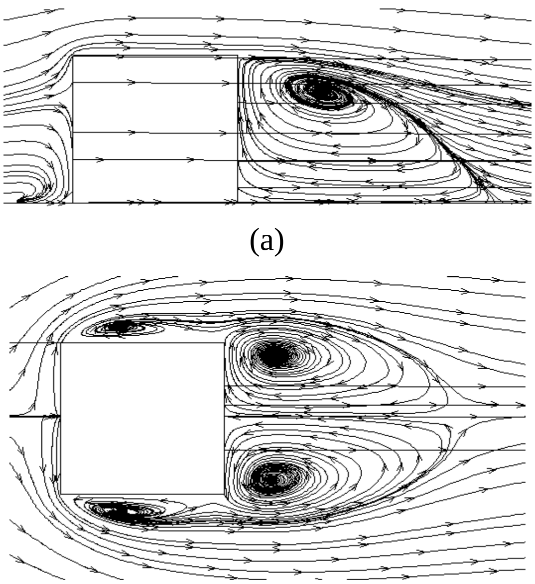

(a)

(b)

Fig. 2-9 Streamtraces predicted by *k*-*ε* standard model, (a) vertical symmetry plane; (b) horizontal plane at 0.125h

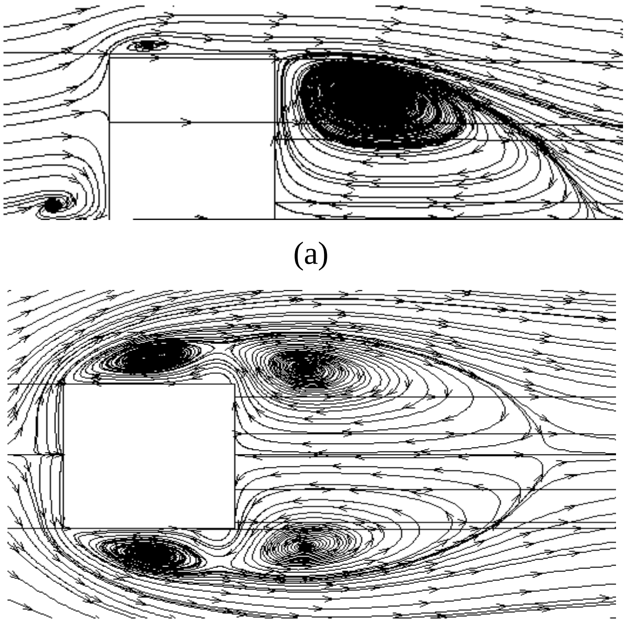

(a)

(b)

Fig. 2-10 Streamtraces predicted by *k*-*ε* RNG model, (a) vertical symmetry plane; (b) horizontal plane at 0.125h

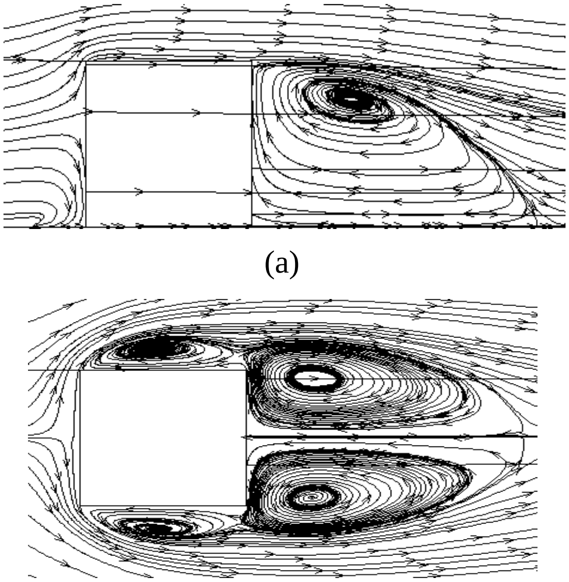

(a)

(b)

Fig. 2-11 Streamtraces predicted by *k*-*ε* Realizable model, (a) vertical symmetry plane; (b) horizontal plane at 0.125h

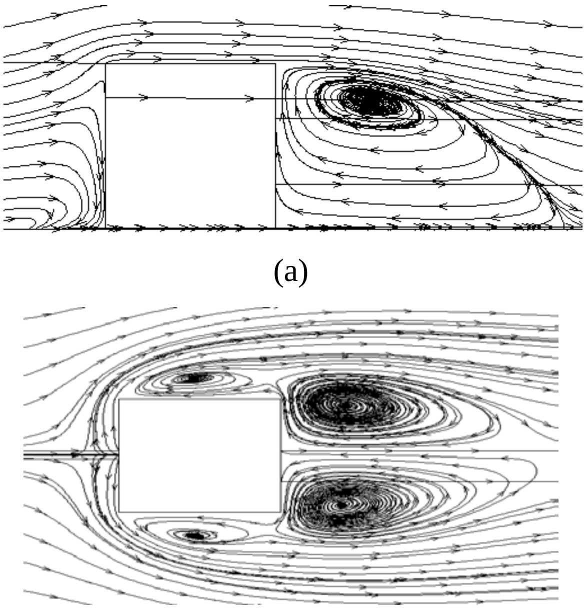

(a)

(b)

Fig. 2-12 Streamtraces predicted by *k*-*ω* standard model, (a) vertical symmetry plane; (b) horizontal plane at 0.125h

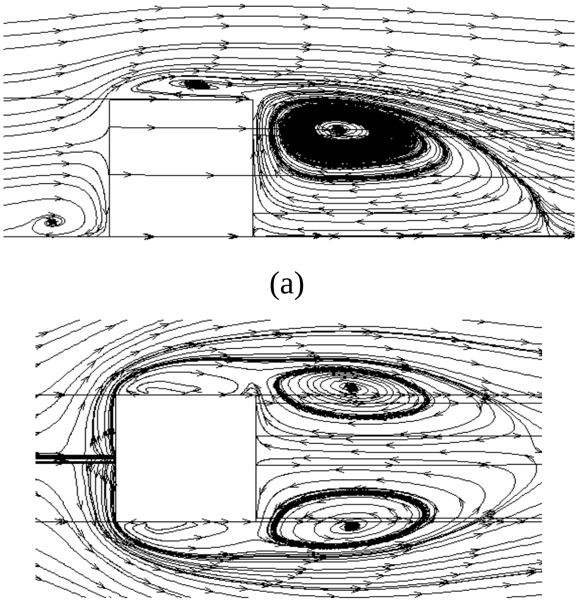

(a)

(b)

Fig. 2-13 Streamtraces predicted by k-ω-SST model, (a) vertical symmetry plane; (b) horizontal plane at 0.125h

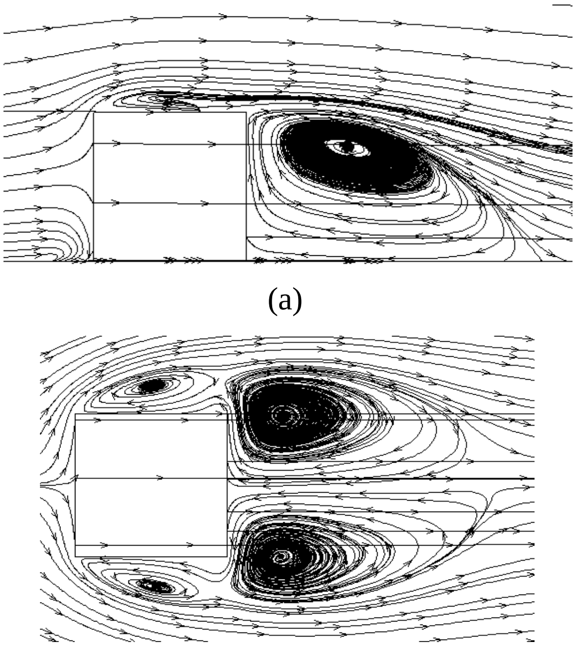

(a)

(b)

Fig. 2-14 Streamtraces predicted by Reynolds Stress Model, (a) vertical symmetry plane; (b) horizontal plane at 0.125h

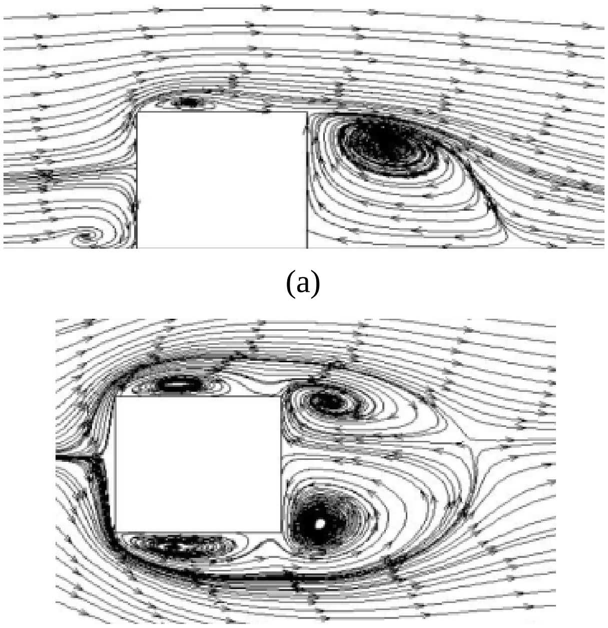

(a)

(b)

Fig. 2-15 Streamtraces predicted by DES-SST model, (a) vertical symmetry plane; (b) horizontal plane at 0.125h

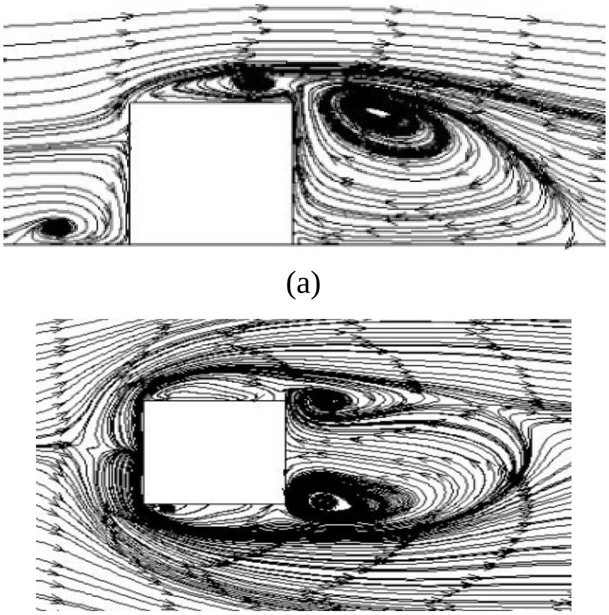

(a)

(b)

Fig. 2-16 Streamtraces predicted by LES (dynamic Smagorinsky), (a) vertical symmetry plane; (b) horizontal plane at 0.125h

2.8.3 Flow Recirculation Length

Unfortunately, there is no reported experimental data about the recirculation length for the reattachment behind the cube. The flow recirculation length predicted by different models has been summarized in Table 2.2. From this table, one can see that the recirculation length predicted from the RANS models is larger than that from DES or LES. This observation is consistent with information reported in the literature [27], where the result from LES is closer to experimental data in the case of a square cylinder.

Table 2.2 Flow recirculation length in the wake region (h: cube height)

Model	Recirculation length
Spalart-Allmaras	1.80h
k-*ω* standard	1.75h
k-*ω*-SST	2.25h
k-*ε* standard	1.63h
k-*ε* RNG	1.95h
k-*ε* Realizable	1.85h
Reynolds Stress	1.80h
DES-SST	1.35h
LES (Dynamic Smagorinsky)	1.50h

2.9 Discussion and Conclusions

As mentioned above, there is less information reported in the literature about numerical simulations over cubes with unstructured meshes, for both RANS models and LES. The main reasons may be the ineffective discretization of space with an unstructured mesh and the general lack of familiarity of unstructured meshes in this type of application. Nevertheless, through construction of the computational model and setting up of the mesh, we have found that the unstructured mesh is much more flexible than a structured mesh. However, successful implementation of an unstructured mesh requires good experience using some important mesh parameters, such as cell growth rate, maximum cell size and size function type, etc.

The simulation results from both DES-SST and LES are not as good as those from *k*-*ω*-SST and RSM. This may be due to the fact that the mesh near the cube is still too coarse for the LES case. Usually the y^+ value required for LES is around 1 [22], which consequently requires huge computing power for the high Reynolds number in the current simulations. Although the Werner-Wengle wall function has been implemented, it may be that the mesh is still too coarse to capture the near-wall region with the current mesh methodology. For the DES case, the communication between the RANS model and the LES model at the interface might be an issue affecting the prediction accuracy.

Computational domain size of type A is too small, and the boundary conditions will greatly affect the simulation results on both the roof and leeward side of the cube. Type B, which is recommended by the Best CFD Performance Guide [6], is acceptable for the simulation results when compared with a larger domain size such as type C, since type C domain will only slightly improve the results on the roof region, and does not change the results on either the windward or leeward sides.

Amongst the RANS model mentioned in this chapter, both *k*-*ω*-SST and the Reynolds Stress Model are the most suitable models to predict wind load on a building. They accurately predict the pressure coefficient on the windward wall, the roof and on the leeward wall. The Reynolds Stress Model needs much more computing power than the *k*-*ω*-SST model. The *k*-*ε* standard, *k*-*ε* Realizable and *k*-*ω* standard are not suitable for bluff body flow simulations. Spalart-Allmaras model and *k*-*ε* RNG give similar prediction performance, and compare reasonably well with experimental data.

In this thesis, the velocity field obtained from the numerical simulations has not been compared with experimental data. The velocity field predictions are usually more accurate than the pressure field. However, for the current purpose, the pressure distribution is more important than the velocity field in regards to the final objectives of this thesis. It is also important to keep in mind that both the wind tunnel tests and the numerical simulation are performed on scale models.

CHAPTER 3

Wind Load on a Free Standing Roof in an Atmospheric Boundary Layer

The effects of turbulence modeling on the numerical simulation of wind load on a free standing roof are investigated in this chapter. The main objective is to predict the wind load on the mid-section of a free standing inclined roof, also referred to as a canopy, under atmospheric boundary layer flow. Nine turbulence models are considered, seven Reynolds-Averaged Navier-Stokes (RANS) equation models, Large-eddy Simulation (LES) with dynamic Smagorinsky subgrid model and Detached Eddy Simulation (DES-SST). The RANS models are Spalart-Allmaras (SA), k-ε standard, RNG and Realizable, k-ω standard, k-ω-SST and Reynolds Stress Model (RSM). The difference in mean pressure coefficient (C_p) across the roof, at different wind directions, obtained from each RANS model with two levels of mesh fineness, has been compared with experimental data.

3.1 Flow Problem Description

For the current study, wind tunnel test data corresponding to an atmospheric boundary layer for a suburban terrain has been extracted from literature [8]. A schematic of the flow problem is shown in Fig. 3-1. The full-scale dimension of the canopy is 30 m x 30 m, with roof slope of 22.5^o and support height of 10 m. The model scale in the numerical model is the same as in the wind tunnel test, 1:100. Velocity and streamwise turbulence intensity profiles at the location of the canopy, but without the presence of the canopy, are shown in Fig. 3-2 and Fig. 3-3, respectively. For consistency with the experiments, the velocity in Fig. 3-2 is normalized by the velocity at 60 m in real scale, u_{60}. Numerically simulated results from k-ω-SST and RSM have been included for comparison.

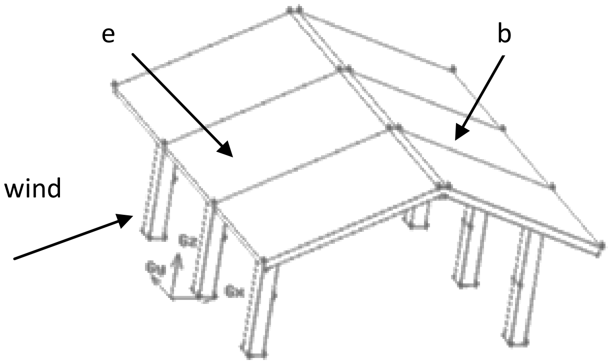

Fig. 3-1 Geometry of canopy with 0^o wind attack angle

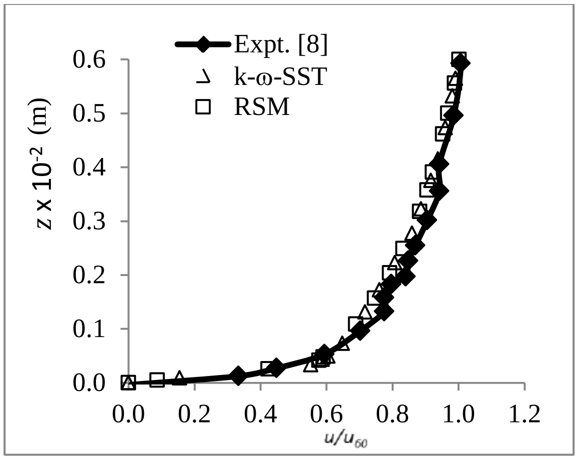

Fig. 3-2 Velocity profile near canopy location

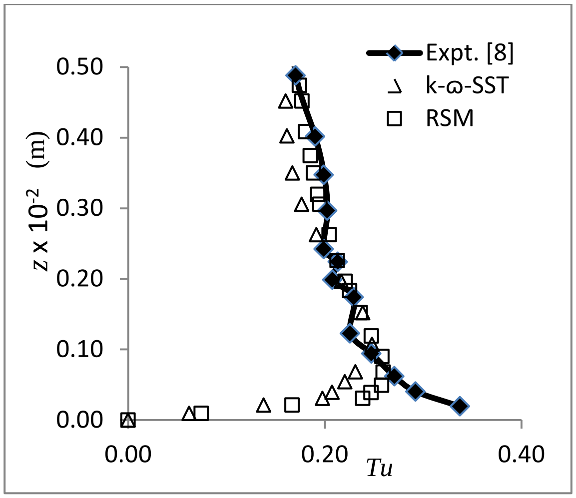

Fig. 3-3 Turbulence intensity profile in streamwise direction near canopy location

3.2 Governing Equations

The equations that govern the unsteady flow of an incompressible fluid are [35]

$$\frac{\partial u_i}{\partial x_i} = 0 \tag{3-1}$$

$$\rho \frac{\partial u_i}{\partial t} + \rho \frac{\partial (u_j u_i)}{\partial x_j} = -\frac{\partial p}{\partial x_i} + \frac{\partial}{\partial x_j}(\mu \frac{\partial u_i}{\partial x_j}) \tag{3-2}$$

where u_i, p, ρ and μ denote the velocity components in the Cartesian coordinate system x_i, (i = 1, 2, 3), pressure, density and dynamic viscosity, respectively.

These equations are the same as those used in Chapter 2. A discussion of the turbulence models used with these equations can be found in section 2.2 and a detailed description of these models is given in Appendix A. Discussion of the wall treatment and implementation of different models is provided in Appendix B.

3.3 Computational Domain

The horizontal and cross-section layouts of the computational domain are illustrated in Fig. 3-4 and Fig. 3-5, respectively, where h is the height of the canopy support.

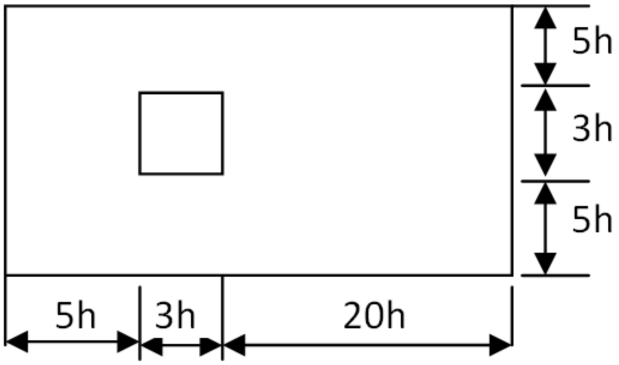

Fig. 3-4 Computational domain (horizontal layout, not to scale)

3.4 Boundary Conditions

The boundary conditions associated with the flow over the canopy are identical to those for flow over the cube building. These conditions are discussed in section 2.5 and mathematically formulated as equations (2-3) to (2-7).

3.5 Mesh Topology

A tetrahedral mesh, with two levels of refinement, is used for the RANS models. For the coarse mesh, the smallest cell size is around 15 mm in the region near the canopy, while in the far region the cell size is around 70 mm, with total cell number of approximately 150,000. For the finer mesh, the smallest cell size is around 7 mm in the region close to the canopy, with 70 mm cell size farther away, with a total of approximately 300,000 cells. The DES and LES models will only be implemented on the coarse mesh due to the computational power limitation. The fine mesh (7 mm) in the vicinity of the canopy is shown in Fig. 3-5.

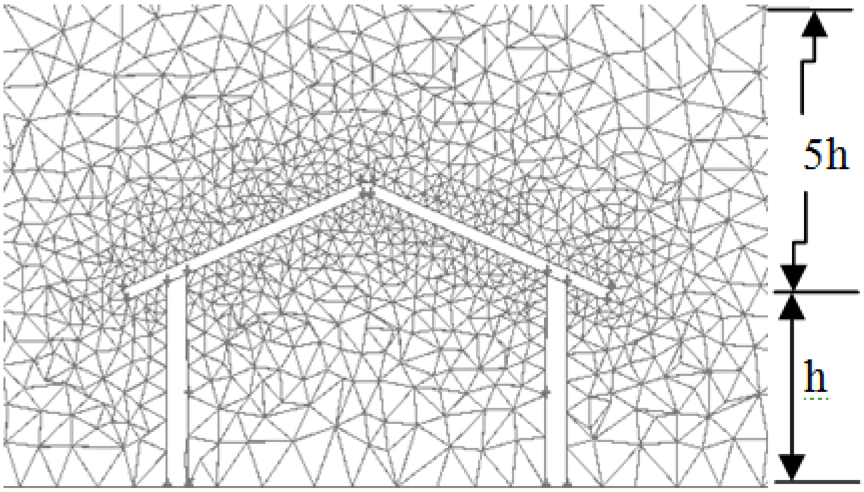

Fig.3-5 Tetrahedral mesh around the canopy in the cross-section layout

3.6 Numerical Setup

The numerical setup for this problem is the same as that for the cube building in Chapter 2. Except for RSM, the convective terms in the RANS models are discretized with third-order accuracy. Second-order accuracy is used for the pressure interpolation and the solution algorithm uses pressure based, pressure-velocity coupling. For RSM, the second-order upwind scheme is used for convection terms, while the solution algorithm uses pressure based, segregated and SIMPLE [24]. Bounded central differencing is used for momentum equations in the LES and DES simulations. The time discretization is implicit second-order. The drag coefficient and a continuity equation residual less than 10^{-7} have been used as the converge criteria.

3.7 Simulation Results

3.7.1 Wind Load on the Canopy Roof

Throughout this chapter, the pressure coefficient refers to the area-averaged pressure coefficient. The pressure coefficient difference on the middle section of the windward roof, i.e., on plate e in Fig. 3-1, with wind attack angles from 0^o to 180^o, has been predicted using the seven RANS models, as well as the DES-SST model and the LES dynamic Smagorinsky model. The pressure coefficient difference, $\Delta C_{p,}$ is defined as the difference between the pressure coefficient on the top surface and on the bottom surface of the roof, that is

$$\Delta C_p = \frac{(p_T - p_B)}{\frac{1}{2}\rho u_{ref}^2} \tag{3-3}$$

where p_T and p_B are the area-averaged pressures on the top and bottom of the roof, respectively. Positive ΔC_p means that the roof plate experiences a downward force, while a negative ΔC_p indicates an upward force.

a). Simulation results from *k-ω*, *k-ω*-SST and Spalart-Allmaras (SA) model

The variations of ΔC_p on plate e, extracted from the coarse mesh simulations (15 mm cell size around the canopy) using the *k-ω* standard, *k-ω*-SST and Spalart-Allmaras models, are plotted in Fig. 3-6, demonstrating that the *k-ω*-SST and Spalart-Allmaras models have much better accuracy than the *k-ω* standard model in the windward attack direction (from 0^o to 90^o). The *k-ω*-SST and SA simulation results at these wind attack angles display good agreement with the experimental data of Ginger and Letchford [8], except for wind in the 0^o angle of attack direction. At leeward attack angles (from 90^o to 180^o), *k-ω*-SST and SA show around 25% deviation from experimental data. The *k-ω* standard model results are even less reliable, as seen in Fig. 3-6.

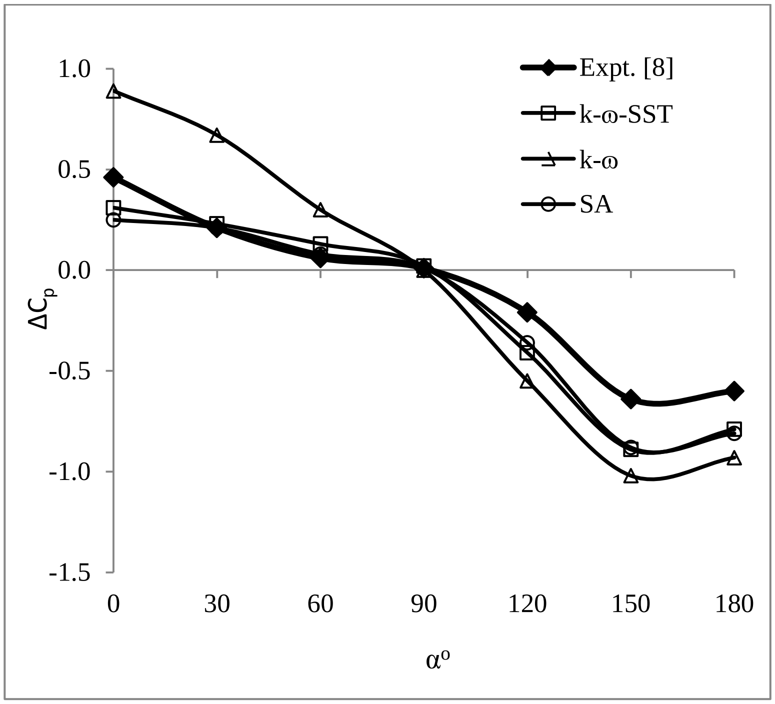

Fig. 3-6 ΔC_p at different wind attack angles predicted by RANS models (coarse mesh near the canopy)

With a finer mesh (7 mm cells around the canopy), *k-ω*-SST and SA models show no improvement at windward attack angles. Figure 3-7 illustrates that, although the *k-ω* standard model shows noticeable improvement, particularly at 0^o, it still deviates much more from experimental data compared to the other two models. On the leeward side, all three models show obvious improvement only at 180^o attack angle. Among these three models, the *k-ω*-SST shows slightly better prediction than the SA model, and much better than the *k-ω* standard model. It yields good prediction at wind attack angles from 30^o up to 90^o, then starts to deviate from the experimental data from 90^o and reaches maximum deviation at 150^o wind attack angle, after which the difference decreases. At 180^o, the *k-ω*-SST model gives good prediction of ΔC_p. In both levels of mesh refinement, all the models show the correct ΔC_p prediction at 90^o wind attack angle. As seen in Fig. 3-7, none of these three models show improvement with mesh refinement at wind attack angles around 150°.

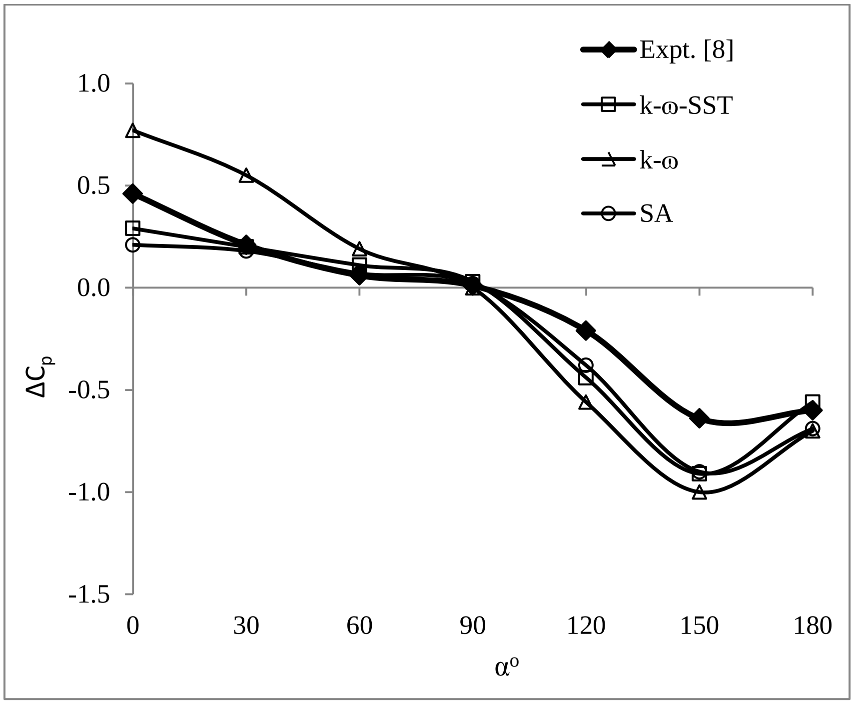

Fig. 3-7 ΔC_p at different wind attack angles by RANS models
(fine mesh near the canopy)

b). Simulation results from *k-ε* standard, *k-ε* RNG, *k-ε* Realizable and Reynolds Stress Model (RSM)

Figure 3-8 illustrates the coarse mesh results for this family of *k-ε* models and RSM. The behaviour of RSM is quite different from the *k-ε* models. At windward attack angles between 0° and 60°, both RSM and *k-ε* standard show significant deviation in the ΔC_p values from the experimental data, while *k-ε* RNG gives relatively better prediction and Realizable gives reasonably good results. In the leeward wind attack angles from 90° to 180°, the RSM model gives much better prediction than the other three models, but the difference between the RSM results and experimental data is still noticeable, especially for wind attack angles between 120° to 180°. The *k-ε* standard model gives the least accurate prediction among the four models.

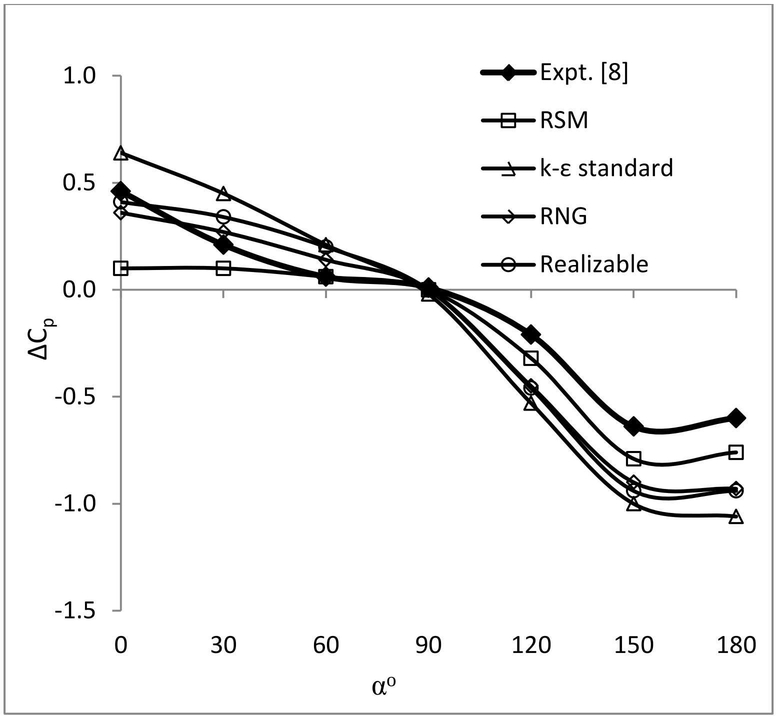

Fig. 3-8 ΔC_p at different wind attack angles by RSM, *k-ε* standard, RNG, Realizable (coarse mesh near the canopy)

Using the finer mesh, there is no improvement in the simulation results of RSM for wind direction from 0^o to 60^o. As seen in Fig. 3-9, *k-ε* RNG and *k-ε* Realizable improve at 30^o and 60^o, but still deviate at 0^o. None of these models can accurately capture the ΔC_p variation with the change of wind attack angle. The simulation result of *k-ε* standard has improved with the refined mesh. In leeward wind attack angles, the RSM results show improvement only at 180^o. The simulation results from *k-ε* RNG and *k-ε* Realizable do not improve at any leeward wind attack angle. Figure 3-9 shows that the *k-ε* standard simulation has improved slightly at wind attack angle of 180^o.

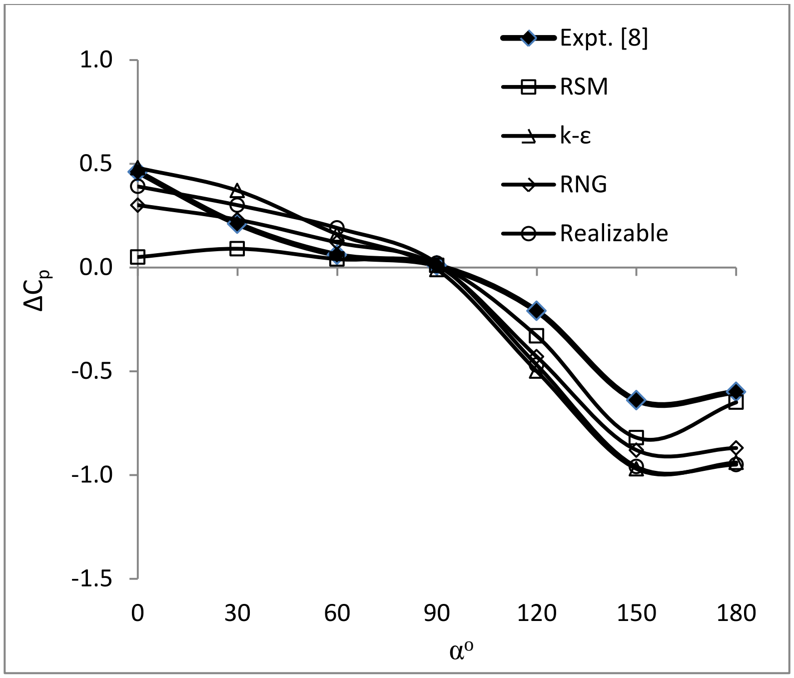

Fig. 3-9 ΔC_p at different wind attack angles by RSM, *k-ε* standard, RNG, Realizable (fine mesh near the canopy)

c). Simulation results from DES-SST and LES

Simulations with DES and LES were conducted only with the coarse mesh (cell size of 15 mm) due to limited computational power. From Fig. 3-10, it seems that neither DES nor LES yields better results than the RANS models. In wind attack angles from 30^o to 180^o, LES does give a better prediction, especially at wind attack angle of 180^o. But, at wind attack angle of 0^o, LES shows much more deviation from the experimental results than DES-SST.

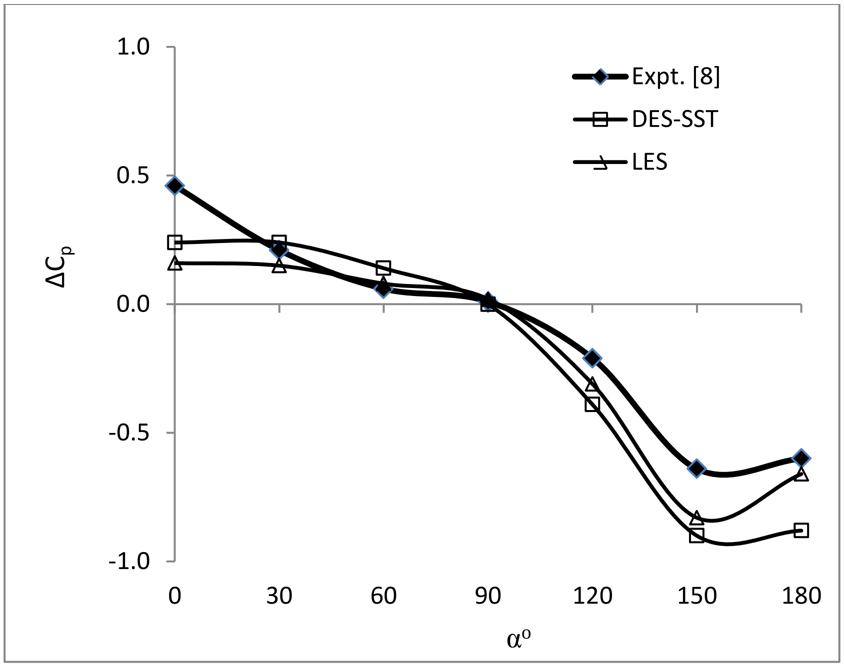

Fig. 3-10 ΔC_p at different wind attack angles by DES-SST and LES (coarse mesh near the canopy)

The ΔC_p difference on plates e and b can be used to determine the drag coefficient and lift coefficient. Using the standard deviation of ΔC_p fluctuations, the peak drag and peak lift can also be calculated by the covariance integration method [8].

The area-averaged mean loads on plates e and b are illustrated in Fig. 3-11 and Fig. 3-12. The drag coefficient is better predicted than the lift coefficient by both DES-SST and LES, and LES performs better than DES-SST. For lift coefficient, the larger deviations from the wind tunnel test results occur at wind attack angles between 0^o and 45^o.

For peak loads on plates e and b, shown in Fig. 3-13 and Fig. 3-14, the drag coefficient is again more accurately predicted than lift coefficient, especially at wind attack angles from 30^o to 90^o. The deviation from experimental data for both the peak drag and lift coefficients at wind attack of 0^o is seen in these figures.

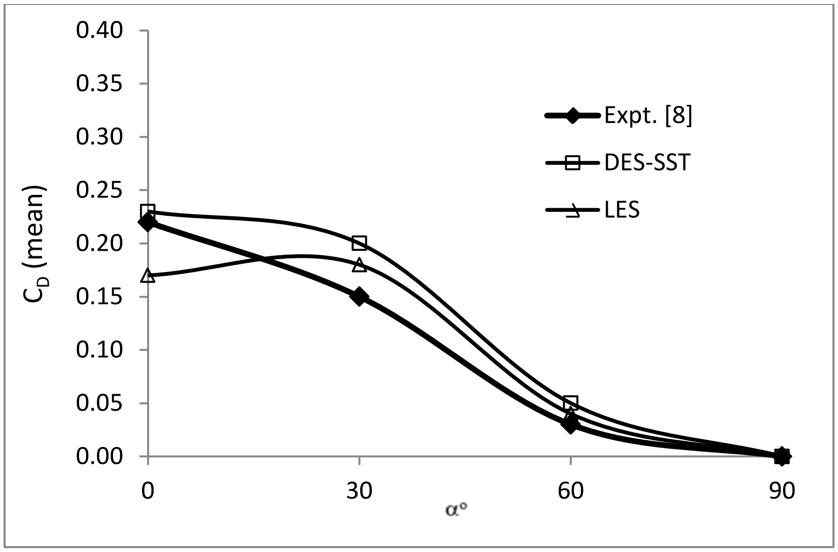

Fig. 3-11 Mean drag coefficient at different wind attack angles by DES-SST and LES (coarse mesh near the canopy)

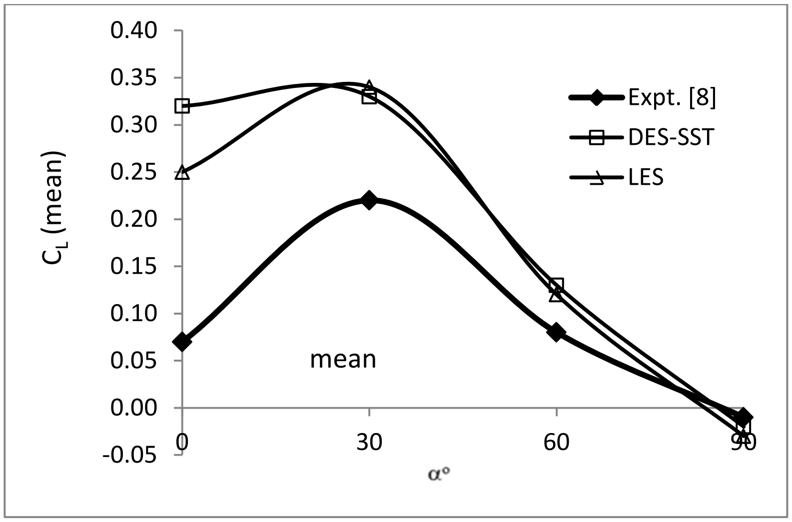

Fig. 3-12 Mean lift coefficient at different wind attack angles by DES-SST and LES (coarse mesh near the canopy)

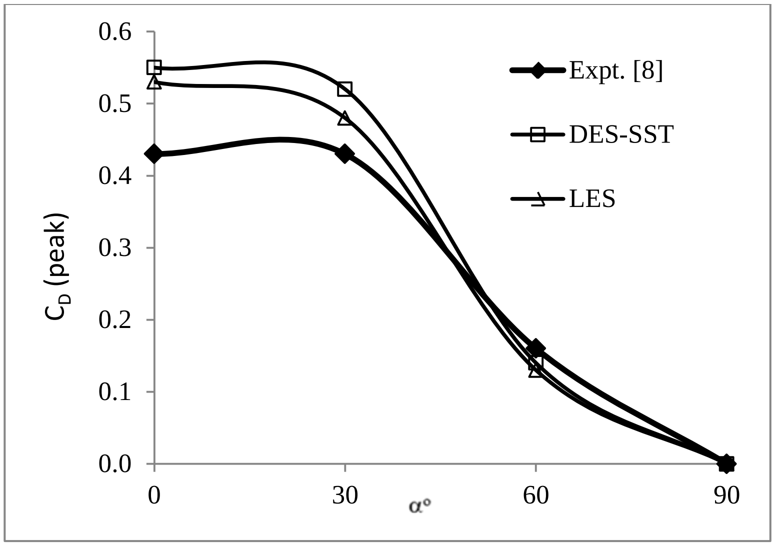

Fig. 3-13 Peak drag coefficient at different wind attack angles by DES-SST and LES (coarse mesh near the canopy)

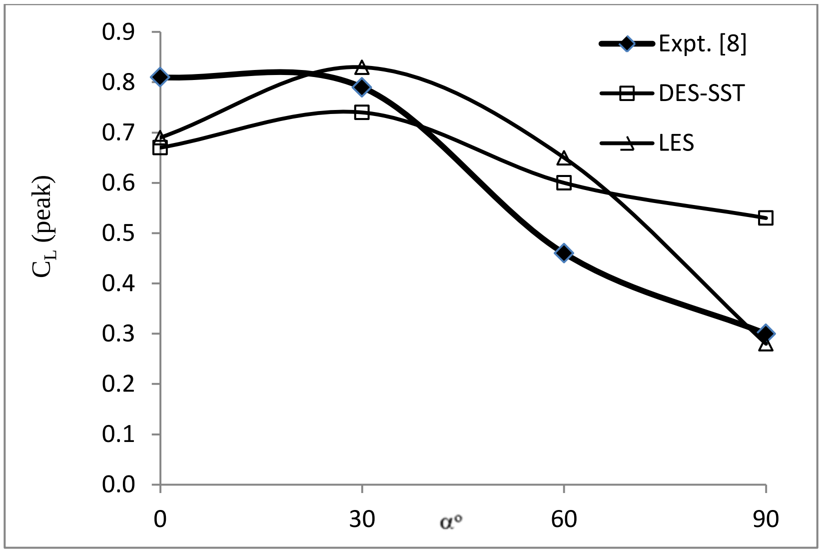

Fig. 3-14 Peak lift coefficient at different wind attack angles by DES-SST and LES (coarse mesh near the canopy)

3.7.2 Velocity Field around the Canopy

Figure 3-15 shows the velocity vector field in the central vertical plane of the canopy from the *k*-ω-SST simulation at wind direction of 0^o. The flow splits when it reaches the front end of the roof, some of the flow moving along the roof top surface without separation at the top leading edge, while some of the flow separates at the bottom leading edge due to the slope of the roof. On the roof top, the flow accelerates as it approaches the roof ridge, and there is no separation occurring in the ridge region. As the air flows along the top surface of the leeward roof, the flow speed decreases, and the flow separates as it approaches the middle of the leeward roof.

Because of the shape of the canopy, there is a large counter-clockwise rotating circulation bubble that forms under the canopy. A downward force and an upward force develop on the windward roof and the leeward roof, respectively. The downward force comes from two sources; one is from the direct contact flow along the top surface, which produces positive pressure due to the slope of roof. The second contribution to the downward force is due to the separated flow at the leading edge of the bottom surface. The upward force also comes from two sources; one is the flow separation on the top surface near the lower part of the leeward roof, the second is the reattachment flow near the lower part of the bottom leeward roof.

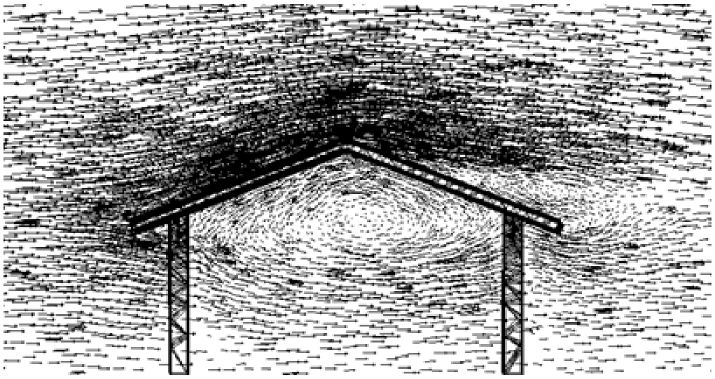

Fig. 3-15 Flow velocity vectors near the canopy at wind attack angle of 0^o, predicted by k-ω-SST

3.8 Discussion and Conclusions

As discussed in section 3.7, there are considerable discrepancies between the experimental data and the computational results for all the turbulence models implemented in this work. There is no uncertainty report by which to assess the validity of the wind tunnel test results. Are the test results really representative of the true wind load on this roof? In the experiments there were only a total of twelve pressure taps for one section of roof, 10 m x 15 m in size, with six pressure taps evenly distributed on the top surface and six pressure taps on the bottom surface. From the plots of pressure coefficient contours on the plates e and b shown in Fig. 3-16 and Fig. 3-17, one can easily observe that the pressure is not evenly distributed on the roof. Since, in the experiments, there are no pressure taps near the edge and ridge regions of the roof, the area-averaged loads calculated from the measurements may not be representative of the real wind loads. This is the main reason for the difference between the numerical simulation and the wind tunnel results.

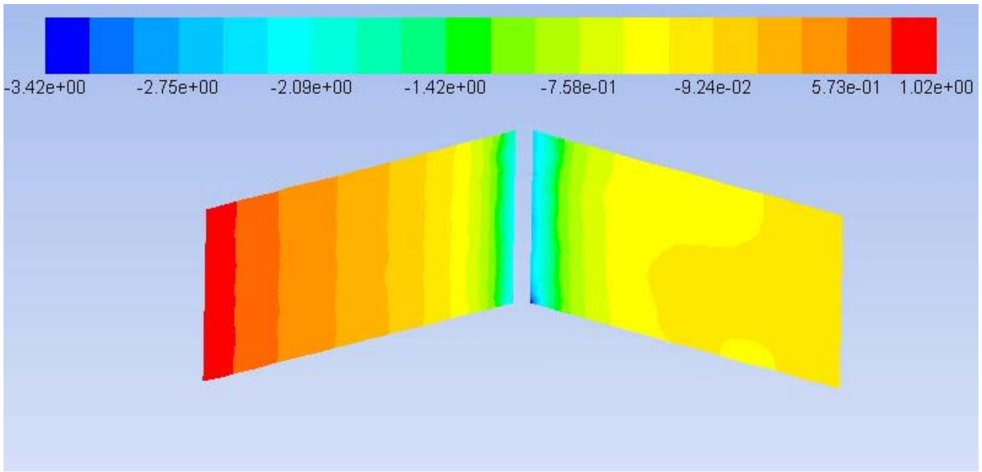

Fig. 3-16 Pressure coefficient contours for top of plate e (left) and plate b (right)

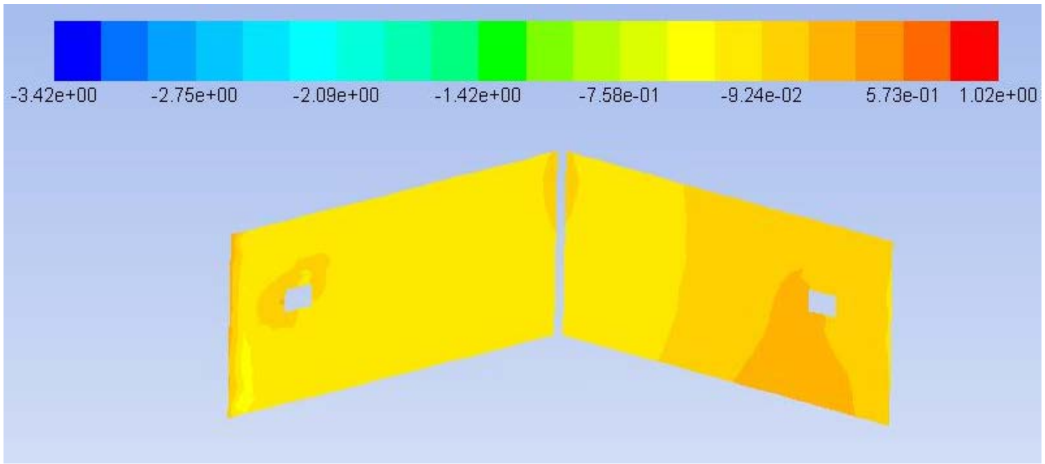

Fig. 3-17 Pressure coefficient contours for bottom of plate e (left) and plate b (right)

The numerical simulations with different turbulence models produce results that vary between each model and between the models and the wind tunnel test results. However, these models show some common features. They all accurately predict the C_p difference at wind attack angle of 90^o (when wind attack angle is parallel to the roof ridge line). They all show significant deviation from the wind tunnel results at wind attack angle of 150^o. The smallest deviation is about 25%, which comes from the RSM and k-ω-SST models. In windward attack angles (from 0^o to 90^o), k-ω-SST, k-ε RNG and SA models show better prediction, while in leeward attack angles (from 90^o to 180^o), RSM shows relatively better results. No model demonstrates good prediction at all wind attack angles. The k-ω-SST model gives slightly better prediction results compared with the other models. Neither DES-SST nor LES improved the simulation results in terms of mean wind load. In the leeward direction, LES gives a slightly better prediction than the DES-SST model. For both DES-SST and LES models, the drag prediction is better than the lift prediction. For peak wind load, LES performs slightly better than DES-SST for both drag and lift coefficient.

CHAPTER 4

Mean and Peak Wind Load on Flat Roof Mounted Solar Panels in an Atmospheric Boundary Layer (Basic Case)

The two validation cases discussed in Chapters 2 and 3 have shown that both k-ω-SST and RSM give better prediction of mean wind loading than other RANS models in bluff body flow, and either DES-SST or LES can be used to simulate both the mean and peak wind load. In this chapter, considering the building dimensions and the geometrical complexity of solar panel arrays, only the k-ω-SST model will be used to predict the mean wind load on solar panels, employing three levels of mesh fineness. DES-SST will be used to predict both mean and peak wind load on the coarsest mesh due to computational power limitations. Wind load will be predicted from these two models with wind attack angles from 360^o to 180^o with increment angle of 30^o. Additionally, wind attack angles of 340^o and 320^o will be tested to disclose the wind load change at the most critical wind attack angle of 330^o (based on our simulations and wind tunnel test results). Wind attack angle of 360^o is defined as wind approaching the rear deflector in the normal direction from the North. The solar panels face towards the South, and the building is aligned in the North-South direction, as illustrated in Fig. 4-1.

4.1 Flow Problem Description

The building is located in suburban terrain following the definition of ASCE 07 [4] ground surface roughness and is categorized as low-rise type with dimensions of 45m x 45m x 9.1m. The roof of the building is covered with arrays of solar panels in the real field situation. The size of a single solar panel is 1.6m x 1.0m with thickness around 50mm. A wind deflector with about 2mm thickness is attached at the back. The tilt angle of the solar panel is 25^o. Figure 4-1 shows a layout of 16 solar panels, concentrated in the corner of the roof, one wind deflector and one solar panel makes one assembly. Only these 16 panel assemblies are simulated in this study due to the computing power limitations and only one corner panel will be monitored for wind load. Wind tunnel tests have shown that the solar panel array at the roof corner experiences much more wind load than in other regions on the roof.

In numerical simulations over surface-mounted objects, the velocity and turbulence intensity continue to develop from the computational domain inlet to the building location. From our simulation experience, it is known that the predicted changes in velocity and intensity profiles depend on mesh style and numerical setup. In order to obtain the correct profiles at the building location, a trial and error procedure has been taken to determine the appropriate turbulent kinetic energy (k) and energy dissipation rate (ε) at the computational domain inlet. Without the presence of the building, the velocity profile and turbulence intensity profile at the building windward wall location from the k-ω-SST simulation are shown in Figs. 4-2 and 4-3, respectively. Wind tunnel test results provided by RWDI [28] have also been included for comparison. In Fig. 4-2, u_{ref} is the reference velocity taken at five feet above the wind tunnel floor and near the building.

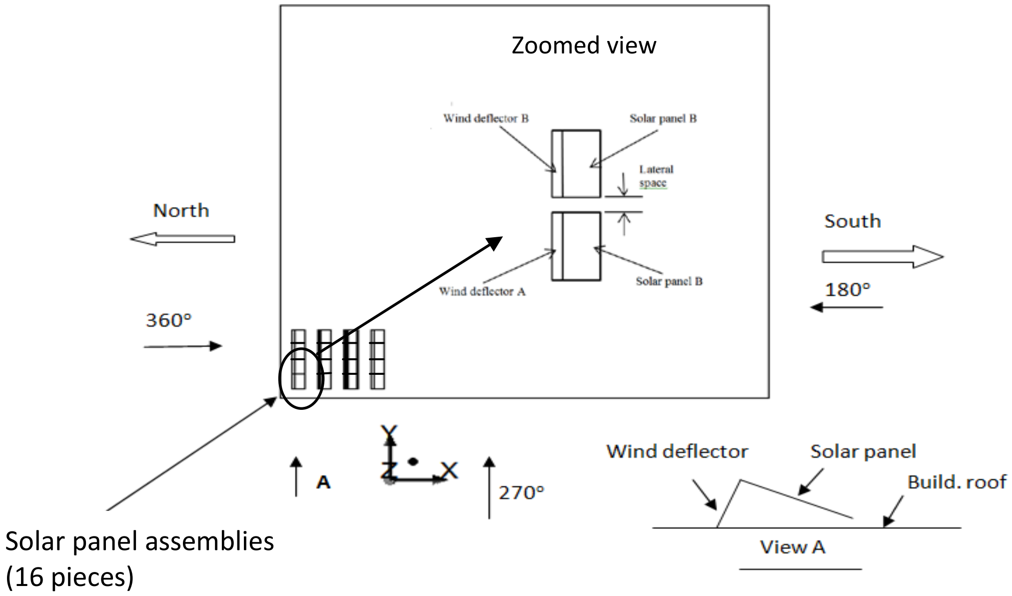

Fig. 4-1 Simulated solar panel layout on a square roof

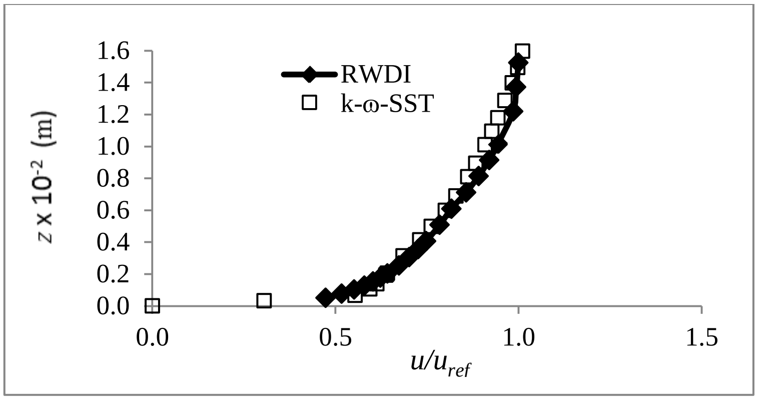

Fig. 4-2 Velocity profile at location of the building, without presence of the building

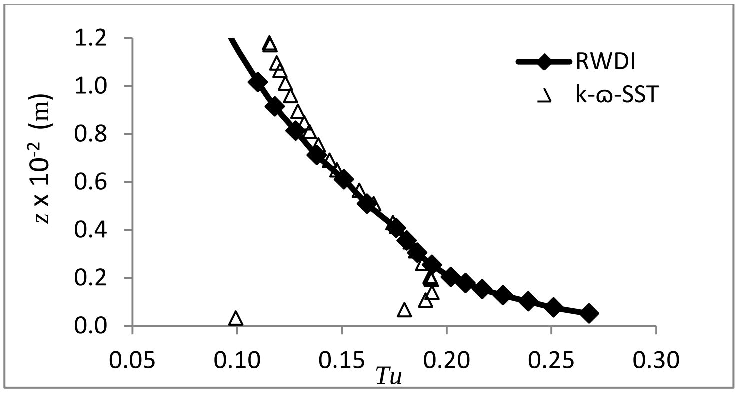

Fig. 4-3 Turbulence intensity in streamwise direction at building location, without presence of the building

4.2 Governing Equations

The equations that govern the unsteady flow of an incompressible fluid are:

$$\frac{\partial u_i}{\partial x_i} = 0 \tag{4-1}$$

$$\rho \frac{\partial u_i}{\partial t} + \rho \frac{\partial (u_j u_i)}{\partial x_j} = -\frac{\partial p}{\partial x_i} + \frac{\partial}{\partial x_i}(\mu \frac{\partial u_i}{\partial x_j}) \tag{4-2}$$

where u_i, p, ρ and μ denote the velocity components in the Cartesian coordinate system x_i (i = 1, 2, 3), pressure, density and dynamic viscosity, respectively.

These equations are the same as those used in Chapter 2. A discussion of the most commonly used turbulence models for these equations can be found in section 2.2 and a detailed description of these models is given in Appendix A. In the present study, only the k-ω-SST (eqns. A-10, A-11) and DES-SST (section A.3) models have been implemented. Discussion of the wall treatment and implementation of different models is provided in Appendix B.

4.3 Computational Domain

The extent of the computational domain in the lateral (y) direction is the same as the distance between the wind tunnel side walls, which is equivalent to 2.5h, where h is the building height. Upstream and downstream lengths are 5h and 20h respectively, while the vertical extent is the same size as the wind tunnel, which is around at 7h. One can refer to Fig. 4-4 for the horizontal layout of the computational domain, and Fig. 4-5 for the vertical elevation layout. Boundary conditions are also included in these figures, where all the walls are modeled as no-slip walls.

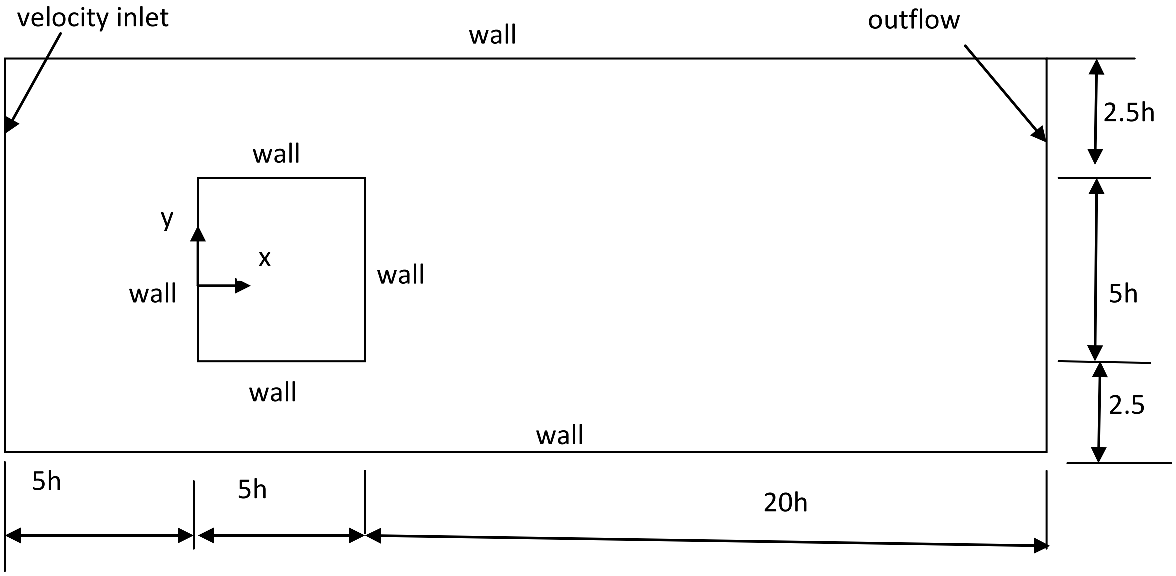

Fig. 4-4 Computational domain horizontal plan layout (not to scale)

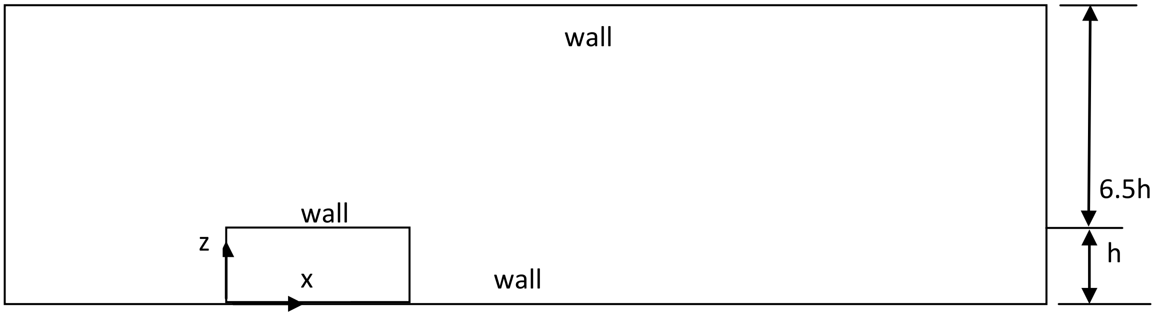

Fig. 4-5 Computational domain vertical plan layout (not to scale)

4.4 Boundary Conditions

The boundary conditions associated with the flow over the solar panels are identical to those for flow over the cube building. These conditions are discussed in section 2.5 and mathematically formulated as equations (2-3) to (2-7). The solar panels themselves are regarded as impermeable solid walls on which a no-slip condition is applied.

4.5 Mesh Topology

Three levels of mesh fineness of a tetrahedral mesh (2, 4 and 8mm cell size in regions near the solar panels) are used for the *k*-*ω*-SST model, while only one level of coarse mesh (8mm) is used for DES due to the limited computing power available. The number of tetrahedral cells for the three levels of fineness are around one million, half million and quarter million for the finest mesh, intermediate mesh and coarsest mesh, respectively. Figure 4-6 shows the finest mesh (2mm) cross-section near the solar panel array.

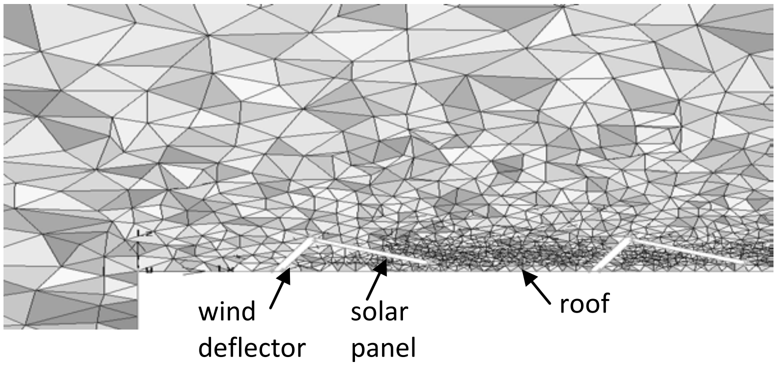

Fig. 4-6 Vertical cross-sectional view of the fine mesh (2mm) around the corner solar panel array

4.6 Numerical Setup

The numerical setup for this problem is the same as that for the cube building in Chapter 2. The convective terms in the k-ϖ-SST model are discretized with third-order accuracy. Second-order accuracy is used for the pressure interpolation and the solution algorithm uses pressure based, pressure-velocity coupling. Bounded central differencing is used for the momentum equations in the DES simulations. The time discretization is implicit second-order. The drag coefficient and a continuity equation residual less than 10^{-7} have been used as the converge criteria.

4.7 Simulation Results

Throughout this chapter, the pressure coefficient refers to the area-averaged pressure coefficient. Similar to the analysis of the flow over a canopy discussed in Chapter 3, the pressure coefficient difference, $\Delta C_{p,}$ is defined as the difference between the pressure coefficient on the top surface and on the bottom surface of the solar panel or wind deflector, that is

$$\Delta C_p = \frac{(p_T - p_B)}{\frac{1}{2}\rho u_{ref}^2} \tag{4-3}$$

where p_T and p_B are the area-averaged pressures on the top and bottom of the panels (or deflectors), respectively. Positive ΔC_p means that the panels/deflectors experience a downward force, while a negative ΔC_p indicates an upward force. Since the solar panels and wind deflectors are at different positions with different slant angles, the wind load on the solar panels and wind deflectors will be different with different wind attack angles. In order to better understand the wind load on the solar panel assembly, it is better to analyze the wind load on the solar panel and wind deflector separately.

4.7.1 Area-averaged Pressure Coefficient Difference for the Solar Panels

From the simulation results (Fig. 4-7), it can be seen that the largest C_p difference occurs at around 320^o, which agrees with the wind tunnel test results. Numerical simulations from all three levels of cell refinement clearly predict the correct C_p difference trend with wind attack angle. The simulation results from k-ω-SST with the fine mesh of 2mm are almost identical to the results with cell size of 4mm. Around the critical wind attack angle (320^o), the simulation results with 8mm cell size deviate from the experimental data much more compared to the results with cells of 2mm and 4mm. Nevertheless, the numerical simulation of C_p with the fine mesh matches well with experimental data at most wind attack angles, except for wind attack at around 320^o, where the deviation from experimental data is about 40%.

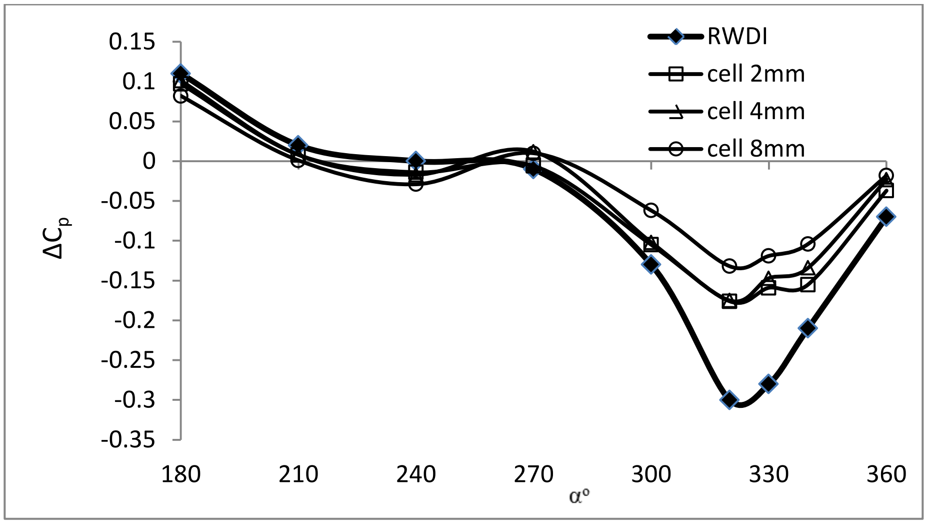

Fig. 4-7 C_p difference on the solar panel predicted by *k*-*ω*-SST

When the wind attack angle reduces from 360^o to 320^o (wind coming from the North and shifting to the Northwest), the solar panel is subjected to more negative C_p difference (i.e., an increasingly upward wind load). This is because the shear layer gets closer to the solar panel as the wind shifts from North to Northwest, which consequently increases the velocity gradient. This can be seen from Fig. 4-8 and Fig. 4-9, which illustrate the velocity vectors of the flow at wind attack angles of 360^o and 320^o, respectively. At wind attack of 320^o, the solar panel experiences its maximum upward wind load. After that, the C_p difference increases (lifting force decreases) until a wind attack angle of 270^o (West wind), where the wind lifting force on the solar panel is around zero. At this position the results are consistent with the canopy case discussed in Chapter 3. For a west wind, the solar panel assembly is located inside a separation bubble, as observed from the velocity field shown in Fig. 4-10. For wind attack angles between 270^o and 210^o (from West to Southwest), the C_p difference remains around zero due to the location of the separation bubble. From 210^o to 180^o (wind attack from Southwest to south), the C_p difference increases significantly. In this situation, the first row now functions as the last row and the solar panel receives flow reattachment, as indicated in Fig. 4-11 which illustrates the velocity vectors at wind attack of 180^o.

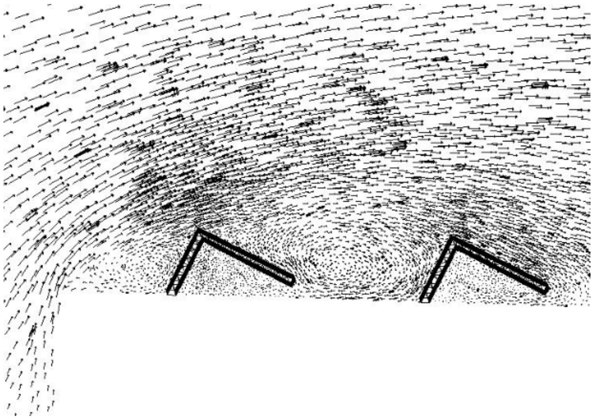

Fig. 4-8 Velocity vectors near the solar panels at 360^o wind attack angle

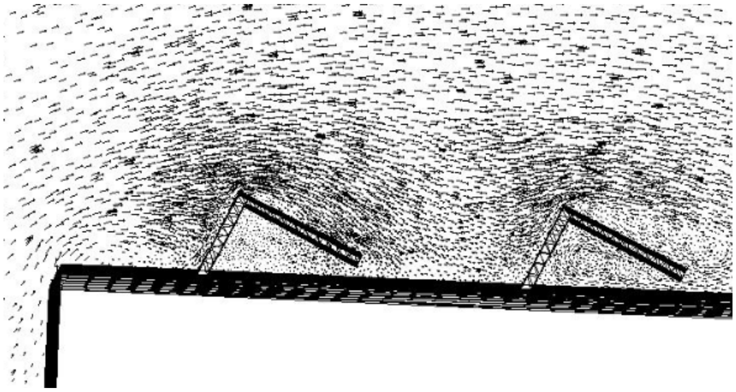

Fig. 4-9 Velocity vectors near the solar panels at 320^o wind attack angle

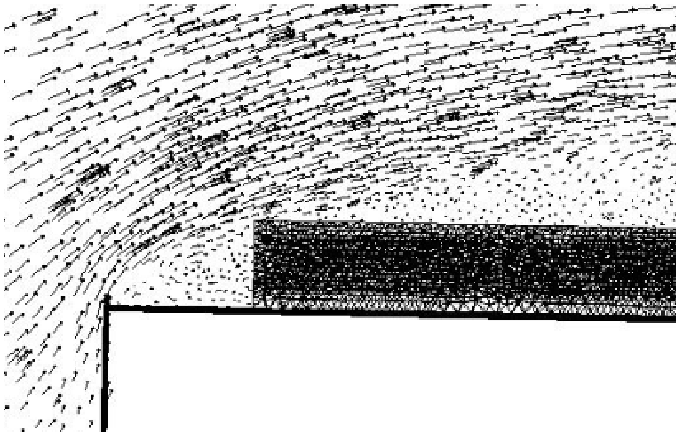

Fig. 4-10 Velocity vectors near the solar panels at 270° wind attack angle

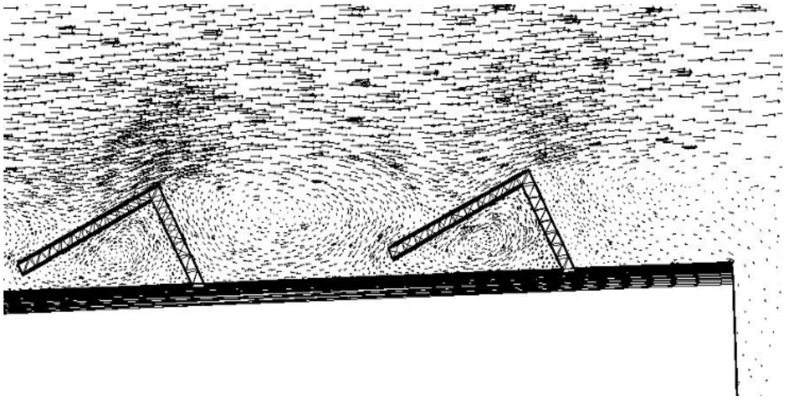

Fig. 4-11 Velocity vectors near the solar panels at 180° wind attack angle

4.7.2 Pressure Coefficient Difference for the Wind Deflector

Due to the wind deflector position which is opposite to that of the solar panel relative to the wind direction, the wind load on the wind deflector is quite different from that on the solar panel. This is clear from a comparison of Fig. 4-7 and Fig. 4-12. In wind attack angle of 360°, both the wind deflector and solar panel receive a slightly upward force (negative pressure coefficient difference). Since the solar panel assembly is located inside the separation bubble, the pressure differences between the top surface and bottom surface are relatively small for both the solar panel and wind deflector. Figure 4-8 shows the velocity vectors at wind attack angle of 360^o. As the wind attack angle decreases from 360^o to 340^o (wind shifting from North towards Northwest), the pressure difference on the wind deflector decreases slightly as the flow on the wind deflector does not change much. Starting from wind attack angle of approximately 340^o, the C_p difference across the wind deflector increases dramatically until wind attack angle of 300^o due to the direct impact of the wind on the wind deflector, as seen in Fig. 4-9. At wind attack of 300^o, the C_p difference reaches its maximum. After that, the C_p difference decreases as the wind attack angle reduces (wind shifting towards West) as the assembly starts to become embedded into the separation bubble. The wind load remains nearly the same (close to zero) for wind attack angles from 270^o towards 210^o because the solar panel assembly is immerged in the separation bubble. Figure 4-10 illustrates the velocity vector field at wind attack angle of 270^o. As the wind continue to shift towards the South, the C_p difference on the wind deflector slightly decreases until reaching a wind attack angle of 180^o, where the wind deflector is in the location of its own flow wake region, as seen in Fig. 4-11 for the velocity vectors at wind attack of 180^o.

Comparing to the experimental data, the prediction of wind load on the wind deflector is much better than on the solar panel, particularly around the critical wind attack angle.

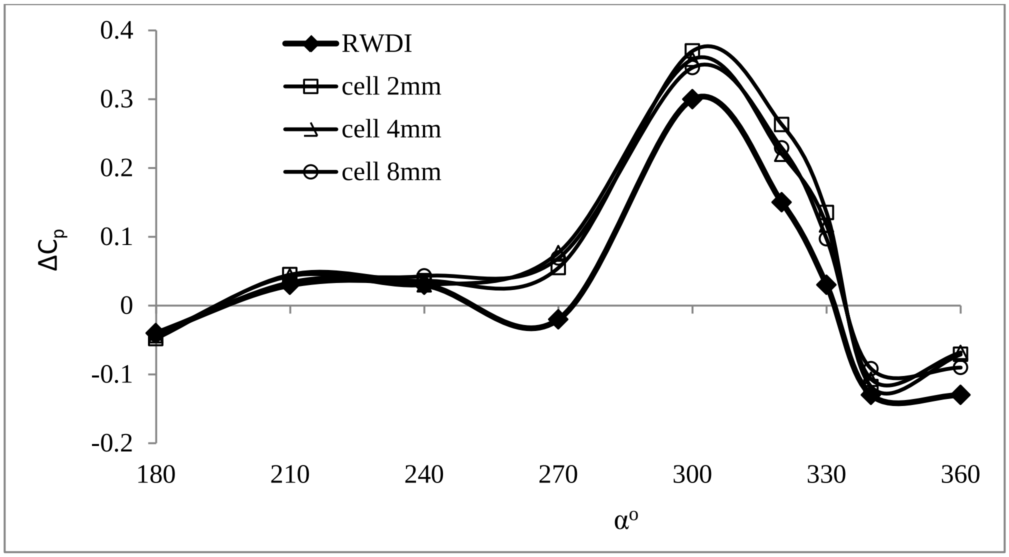

Fig. 4-12 C_p difference on the wind deflector predicted by *k*-*ω*-SST

4.7.3 Drag Coefficient for the Solar Panel Assembly using *k*-*ω*-SST

The wind load on the whole assembly (one solar panel and one wind deflector) is the resultant force from both the wind deflector and the solar panel. Since the solar panel surface area is much larger than the wind deflector surface area, the wind load from the solar panel will make more contribution to the resultant wind load. The results are shown in Fig. 4-13. The drag coefficient of the assembly is negative from wind attack angle of 360^o to 320^o due to the effect of the recirculation bubble on the roof. From wind attack angle 320^o to 340^o, the drag coefficient increases dramatically and reach its maximum at wind attack of 320^o. The reason for this is that more flow impinges directly on both the wind deflector and bottom side of the solar panel as the wind shifts from North to Northwest. After 320^o, the drag coefficient decreases significantly until the wind reaches an angle of 270^o. As the wind attack angle continues to shift, more flow loses direct impact on the assembly. At wind attack between 270^o and 210^o, the drag coefficient is close to 0, as more flow passes parallel to the assembly. After 210^o, the drag coefficient on the assembly increases again until 180^o, since the frontal cross-section area of the assembly increases again. The numerical simulation results for all three levels of cell refinement match well with the experimental data.

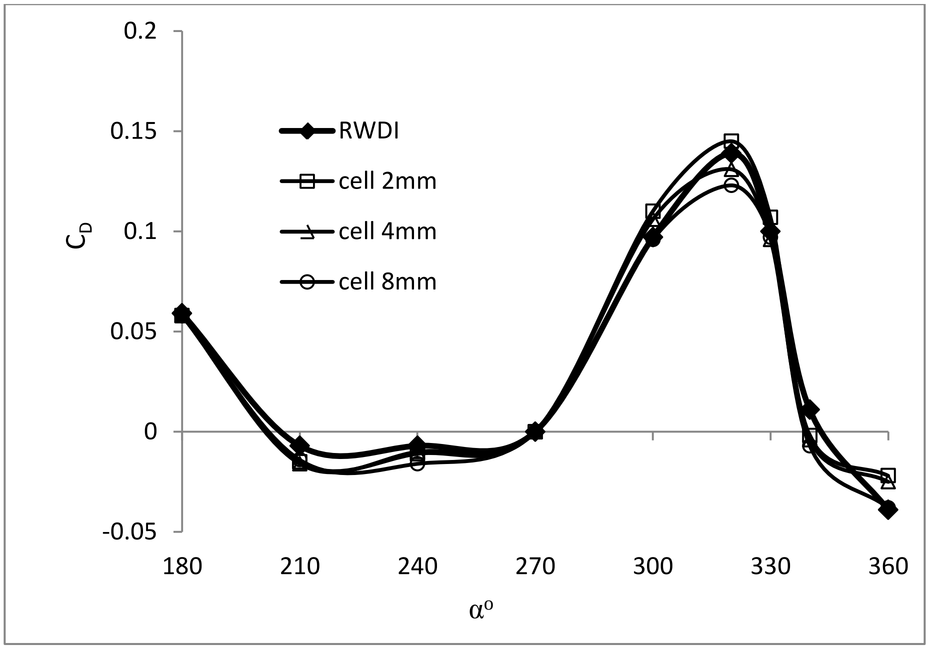

Fig. 4-13 Drag coefficient for the solar panel assembly predicted by *k*-*ω*-SST

4.7.4 Lift Coefficient for the Solar Panel Assembly using *k*-*ω*-SST

The lift coefficient of the whole solar panel assembly increases as the wind attack angle reduces from 360^o to 320^o, as illustrated in Fig. 4-14, and reaches maximum value at wind attack angle of 330^o. As explained in section 4.7.1, this is caused by the shear layer getting closer to the solar panel as the wind attack angle shifts from North to Northwest. At about 320^o, the value of the lift coefficient starts to decrease. This decrease continues from wind attack angle of 320^o to 300^o, where it then maintains a value around zero until wind attack angle of 210^o. Beyond that, the lift coefficient decreases due to the reattached flow on the solar panel. The numerical simulations with mesh cell size of 2mm and 4mm give similar values at all wind attack angles, while the larger cell size of 8mm shows more deviation from the experimental values. Overall, the numerical simulations provide a good match with the experimental data, except at wind attack angle around 330^o.

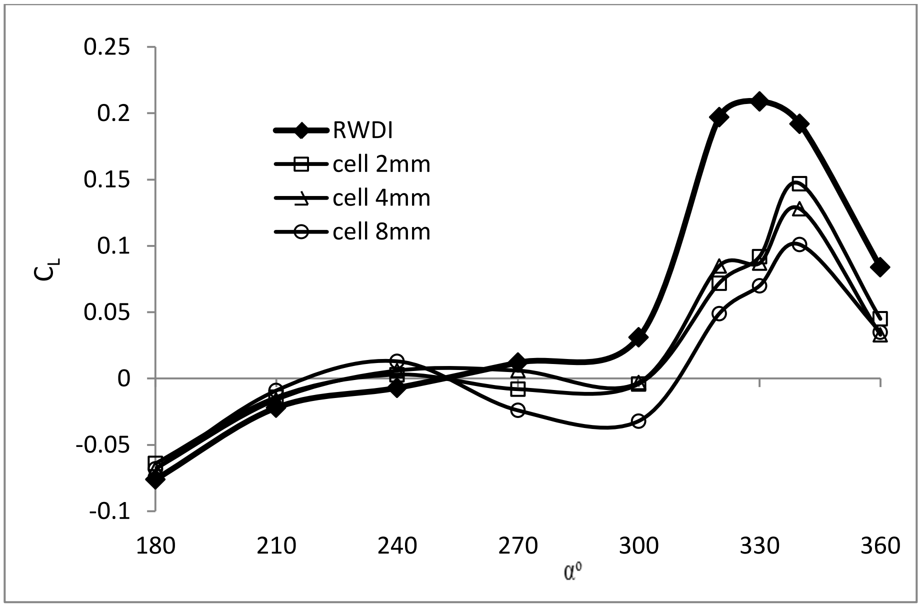

Fig. 4-14 Lift coefficient for the solar panel assembly predicted by *k*-*ω*-SST

4.7.5 Mean Drag Coefficient for the Solar Panel Assembly using DES-SST

The drag coefficient prediction for the complete assembly using DES-SST is less accurate than obtained by using the *k*-*ω*-SST model, as observed by comparing Fig. 4-13 and Fig. 4-15. The predicted mean drag coefficient is in good agreement with the experimental values for most wind attack angles, except at wind attack angles in the range of 320° and 360°. This is likely due to the fact that the 8mm size mesh may be too coarse for accurate simulation using the DES-SST model over the complete range of wind directions.

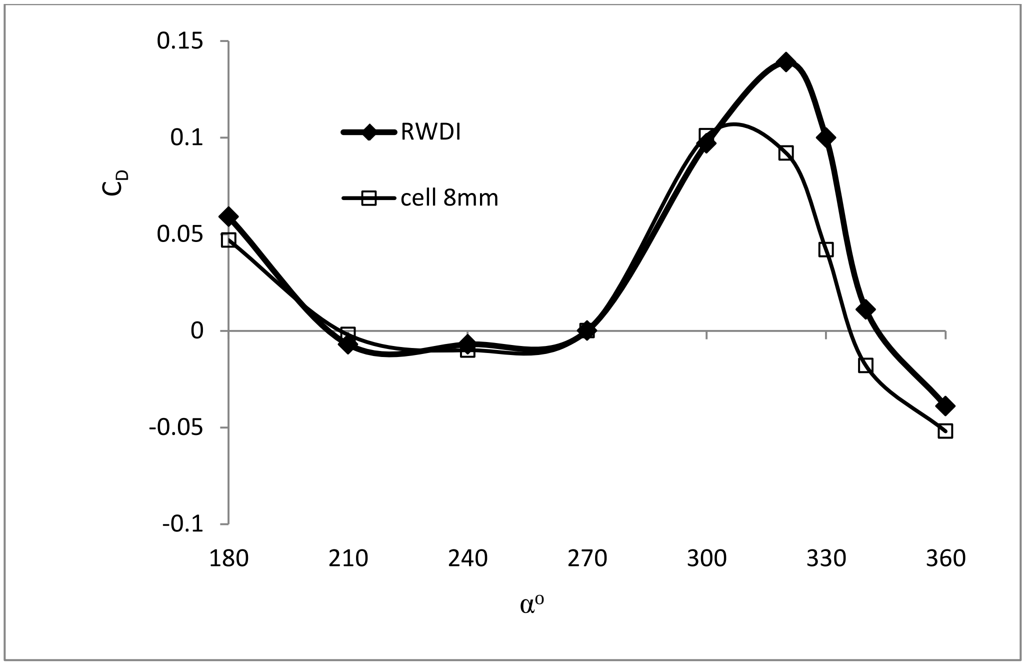

Fig. 4-15 Mean drag coefficient for the solar panel assembly predicted by DES-SST (with coarse mesh)

4.7.6 Mean Lift Coefficient for the Solar Panel Assembly using DES-SST

The mean lift coefficient prediction for DES-SST is also less accurate compared with the prediction from *k*-*ω*-SST model, as seen from a comparison of Fig. 4-14 and Fig. 4-16. It is clear from Fig. 4-15 and Fig. 4-16 that the drag is easier to predict with DES-SST than the lift. It is also evident that the 8mm mesh is too coarse for an accurate DES-SST simulation.

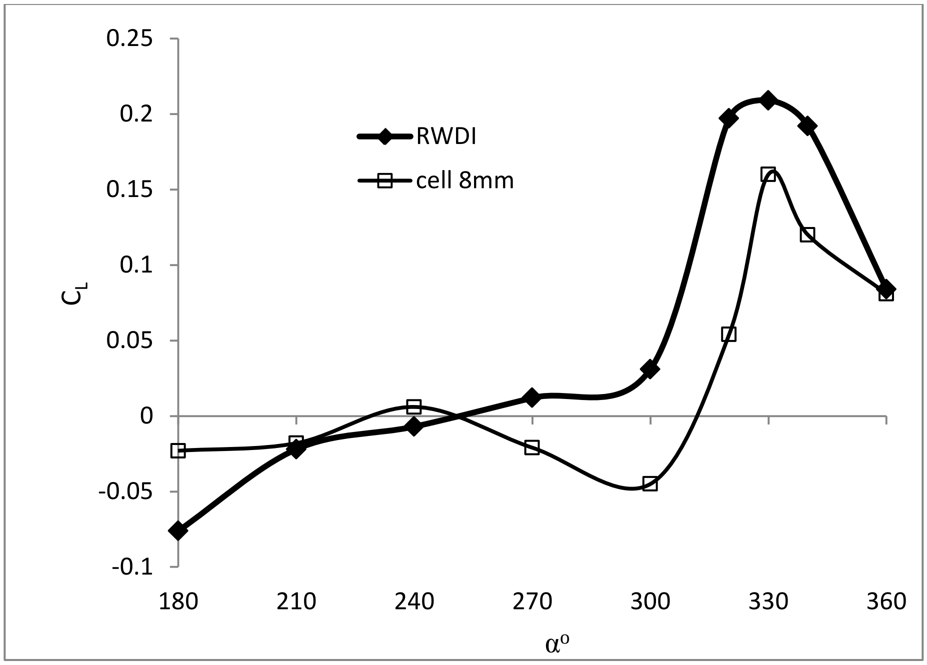

Fig. 4-16 Mean lift coefficient for the solar panel assembly predicted by DES (with coarse mesh)

4.7.7 Peak Drag Coefficient for the Solar Panel Assembly using DES-SST

The prediction of peak drag coefficient has a good match with experimental data except at wind attack angle of 240° (see Fig. 4-17). The peak drag coefficient is caused by fluctuations of the wind load. The deviation from experimental data is likely the result of two main factors; one is that the mesh is too coarse, the second is that the turbulence model itself may not accurately represent the complicated flow phenomena in the vicinity of the solar panel assembly.

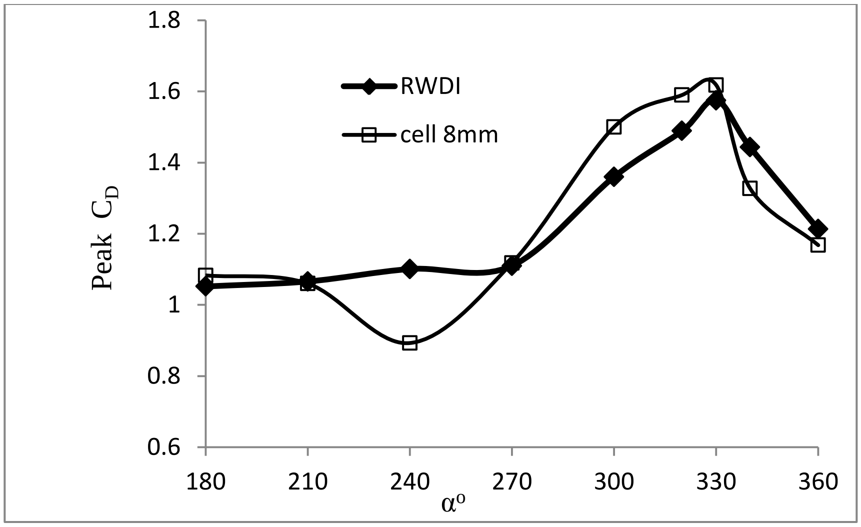

Fig. 4-17 Peak drag coefficient for the solar panel assembly predicted by DES (with coarse mesh)

4.7.8 Peak Lift Coefficient for the Solar Panel Assembly using DES-SST

The prediction of the peak lift coefficient does not agree with the experimental results, although the model does predict the correct trend of the peak lifting force, as seen in Fig. 4-18. The reasons for these inaccuracies are similar with prediction of the peak drag, as explained above.

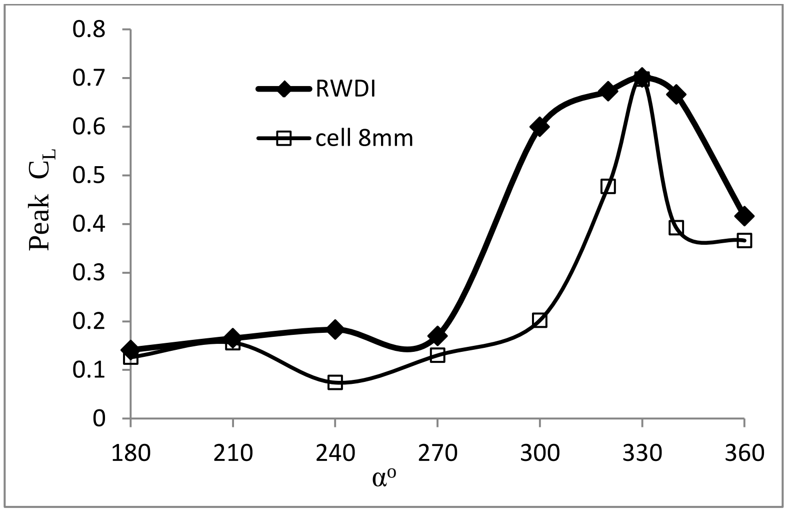

Fig. 4-18 Peak lift coefficient for the solar panel assembly predicted by DES (with coarse mesh)

4.8 Discussion and Conclusions

Even though there is no uncertainty analysis about wind tunnel test result, and the test results should be viewed with some trepidation, we still can draw some conclusions from the current study.

For drag coefficient prediction, the numerical simulation from *k*-*ω*-SST has a good match with the experimental data at most wind attack angles, with three levels of cell fineness. However, for lift coefficient, the simulation is not as good. The numerical simulation results from cell sizes of 2mm and 4mm are similar, and closer to the experimental data when compared with the results from the 8mm cell mesh, and the numerical simulation has a good match with experimental data at all wind attack angles except 330^o. There are couple reasons why this occurs. First, the uncertainty level of the wind tunnel test results, which has not been reported, is unknown. Second, one can question whether the number of pressure taps used in the experiments are enough for capturing the essential flow features (a total of six pressure taps for one solar panel, four in the top surface and two in the bottom surface). Third, the quality of tetrahedral mesh may not be adequate enough to ensure accurate simulation results. Finally, the capability of the turbulence model to capture the key turbulence characteristics of this flow has to be considered.

DES did not improve the simulation results for the mean wind load compare with those from *k*-*ω*-SST. The prediction of the peak drag matches well with experimental data, except at wind attack angle of 240^o, and the prediction of peak drag is much better than the peak lift.

CHAPTER 5

Mean Wind Load on Roof Mounted Solar Panel Arrays in an Atmospheric Boundary Layer (Other Configurations)

The solar panel basic case simulations performed in Chapter 4 have shown that both *k*-*ω*-SST and DES-SST adequately predict the mean lift and drag coefficients at most wind attack angles, and the maximum peak wind load from the DES-SST model occurs at approximately the same location as the maximum mean wind load (around 330^o). Therefore, in this chapter, the *k*-*ω*-SST model is used to investigate wind load changes if the configuration of the solar panel assembly is altered. Three configurations are investigated: i) the solar panel lateral space is increased from 0.125 inches to 2.5 inches (Case 1), ii) the solar panel vertical distance off the roof is increased by 6 inches (Case 2), and iii) the vertical space between the solar panel and the roof is increased to the same height (2.5 feet) as an installed parapet (Case 3).

The computational domain, boundary conditions and the numerical setup are the same as in the basic case in Chapter 4. The mesh used for both Case 1 and Case 2 has cell size of 2 mm near the solar panel, with a total number of cells reaching around 1 million. For Case 3, the simulations are carried out on a mesh with 6mm cell size near the solar panel and parapet, with a total cell number of around 0.7 million.

5.1 Simulation Results

5.1.1 Drag Coefficient for the Solar Panel Assembly

The effects of the modified configurations described above on the drag coefficient are illustrated in Fig. 5-1.

a). (Case 1) Increase of the lateral space

As seen in Fig 5-1, increasing the solar panel lateral space by 2.5 inches does not change the drag at most wind attack angles, except at angles between 360^o to 330^o, where the drag shows a mild increase.

b). (Case 2) Increase of the vertical space off the roof

Increasing the vertical space between the solar panel and the roof significantly increases the drag at wind attack angles of 360^o to 300^o, while there is negligible or no increase for the remaining wind attack angles. This is due to the fact that an increase in the vertical space causes more flow to directly impinge on the wind deflector, which subsequently increases the drag. Figure 5-2 shows the velocity vectors around the assembly at wind attack angle of 330^o.

c). (Case 3) Increase of the vertical space to the same height as a parapet

Increasing the vertical spacing of the solar panel off the roof to the same level of the parapet has a similar effect as Case 2. However, at wind attack angles from 360^o to 320^o, the drag is slightly lower than in Case 2, while at wind attack angles from 270^o to 180^o, the drag is a little higher than Case 2. The reason is same as in Case 2. Figure 5-3 illustrates the velocity vectors around the panel assembly and parapet at wind attack angle of 330^o.

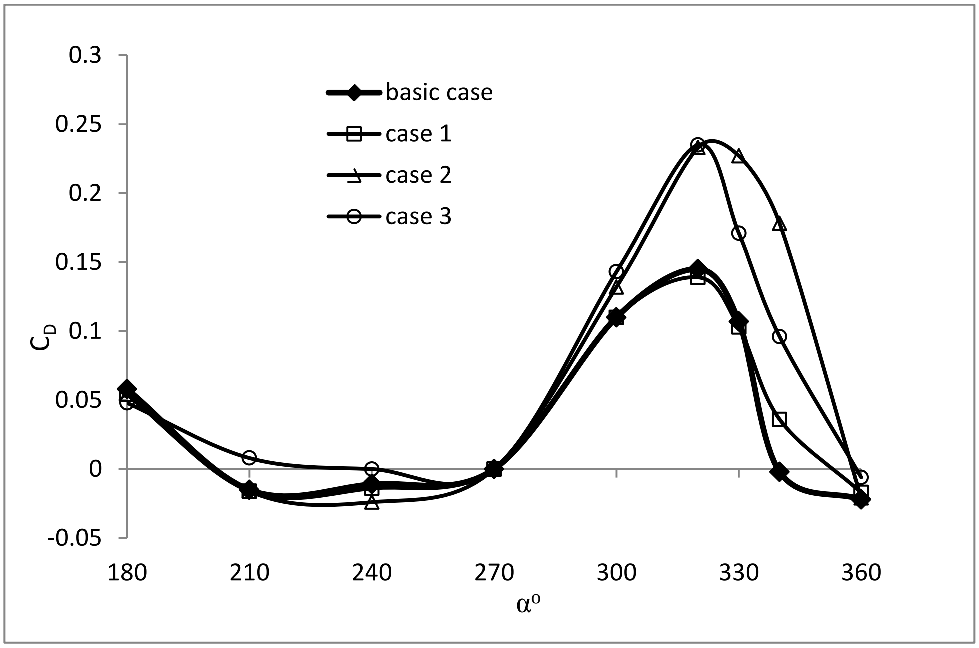

Fig. 5-1 Drag coefficient for three configurations of the solar panel assembly

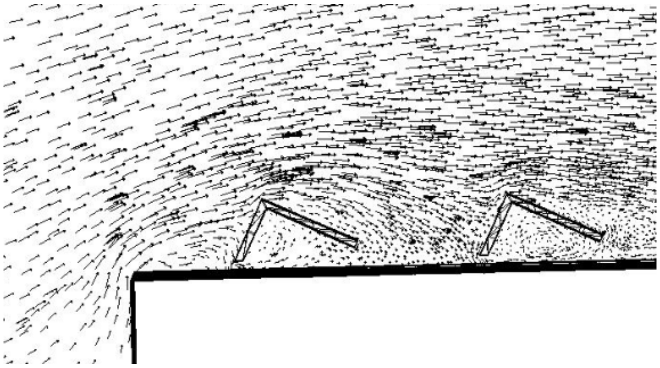

Fig. 5-2 Velocity vector field at wind attack angle of 330^o for vertical spacing of 6 inches off the roof

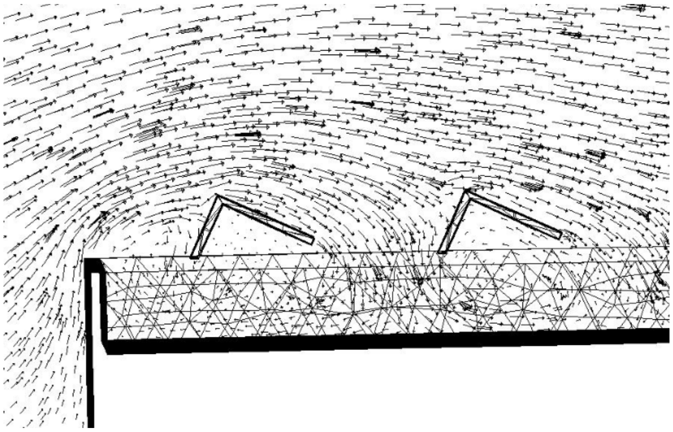

Fig. 5-3 Velocity vector field at wind attack angle of 330^o for vertical spacing at same height as the parapet

5.1.2 Lift Coefficient for the Solar Panel Assembly

The effects of the modified configurations described above on the lift coefficient are illustrated in Fig. 5-4.

a). (Case 1) Increase of the lateral space

Increasing the solar panel lateral space reduces the lift force significantly at wind attack angles between 360^o to 320^o, while at the remaining wind attack angles, the effect is mild. The reason for this may be that the pressure difference between the top surface and bottom surface of both the solar panel and wind deflector decreases due to the ventilation between them.

b). (Case 2) Increase of the vertical space between the solar panel and roof

Increasing the vertical space between the solar panel and roof has a similar effect on the lift force as increasing the solar panel lateral space. It significantly reduces the lift force for wind attack angles between 360^o to 300^o, while the effect on lift is minimal at the remaining wind attack angles. Since an increase in vertical spacing causes more flow to directly impinge on the wind deflector, this direct impact increases the drag force and at the same time produces more downward force (reducing the lift force), consistent with the velocity field for wind attack angle of 330^o seen in Fig. 5-2.

c). (Case 3) Increase of the vertical space between the solar panel and roof to the same height as a parapet

Increasing the vertical space between the solar panel and the roof to the same level as a parapet reduces the lift force significantly at wind attack angles between 360^o to 270^o. The same amount of lift force is maintained at wind attack angles from 270^o to 240^o, and the lift force increases significantly at wind attack angles from 240^o to 180^o. The increase in vertical space to the same level as the parapet causes more flow to directly impact on the wind deflector and more flow reattaches onto the solar panel, subsequently causing an increase in drag and a reduction in lift force on the assembly. The velocity vectors for this case at wind attack angle of 330^o are shown in Fig. 5-3. At a wind attack angle of 210^o, the flow is shielded by the parapet and the lift coefficient increases due to a recirculation flow that develops near the parapet, as seen in Fig. 5-5.

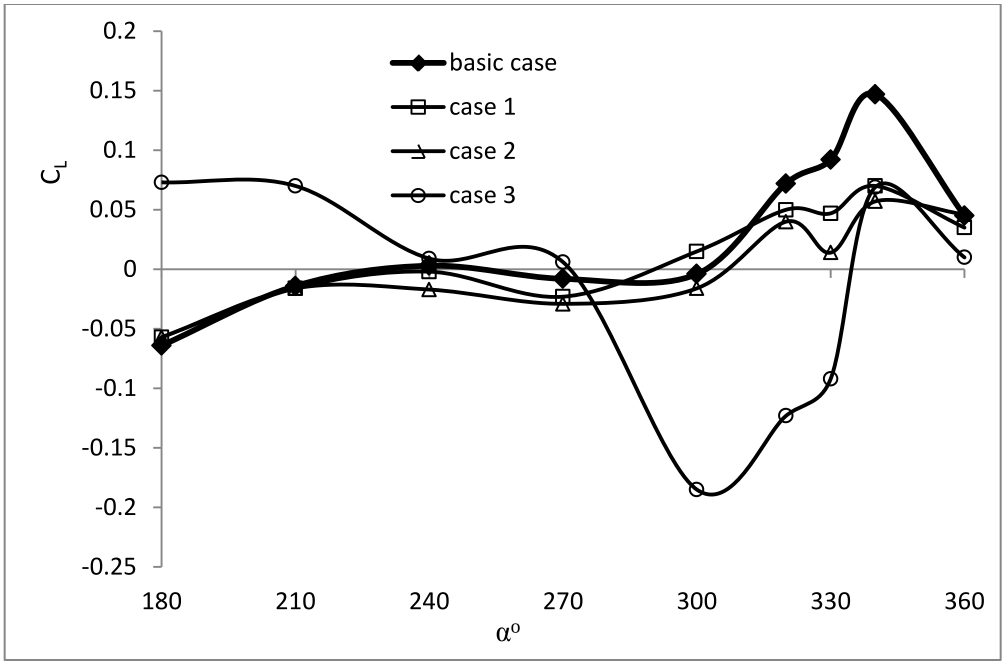

Fig. 5-4 Lift coefficient for three configurations of the solar panel assembly

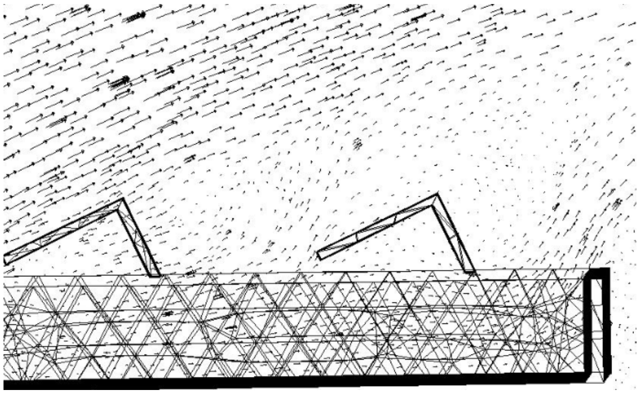

Fig. 5-5 Velocity vectors at wind attack angle of 210° for vertical spacing at the same height as the parapet

5.2 Conclusions

Using the *k*-*ω*-SST model with the same setup as the basic case, results have been obtained for three modified cases. Increasing the solar panel lateral spacing by 2.5 inches does not increase the drag at most wind attack angles, except between wind attack angles of 360° and 330°, where there is a mild drag increase. However, it will significantly reduce the wind lift force between 360^o and 320^o. Increasing the solar panel vertical spacing off the roof by 6 inches increases the drag dramatically for wind attack angles from 360^o to 300^o, while it greatly reduces the lift force at these wind attack angles. Installing the solar panel at the same height above the roof as a parapet increases the drag significantly at wind attack angles from 360^o to 300^o, reduces the lift force for wind attack angles from 360^o to 270^o and increases the lift force for 240^o to 180^o wind attack angles.

CHAPTER 6

Conclusions and Future Work

6.1 Conclusions

In this thesis, the flow over a cube in an atmospheric boundary has been simulated using different computational domains with the *k*-*ω*-SST turbulence model, and the most computationally economic domain size has been identified. With this domain size, seven RANS models, DES-SST and LES models have been tested to predict the pressure coefficient (C_p) distribution. From comparison of simulation results with experimental data, it was determined that the *k*-*ω*-SST and Reynolds Stress models give the best prediction of pressure coefficient distribution on the vertical symmetrical plane, closely matching with experimental data. The Spalart-Allmaras model, *k*-*ε* RNG and *k*-*ε* Realizable models give reasonably good prediction, while the *k*-*ε* standard and *k*-*ω* standard failed to predict the pressure coefficient distribution, especially on the roof and windward face. Neither the DES-SST model nor the LES model with dynamic Smagorinksy option gives better prediction of C_p, contrary to expectations. The reason for this may be that the mesh is not fine enough close to the wall. The flow patterns predicted by each model look similar at first sight, except for the *k*-*ε* standard and *k*-*ω* standard, which fail to predict the rooftop flow separation bubble. However, when closely scrutinized, these flow patterns exhibit some differences. In particular, the wake region recirculation length predicted by the RANS models is longer than that from the DES-SST and LES models, which is consistent with information reported in the literature.

The C_p difference across a canopy in an atmospheric boundary layer has also been predicted with the above-mentioned models. Two levels of mesh fineness have been implemented. No model shows superior prediction performance, but *k*-*ω*-SST demonstrates relatively better prediction. Compared with the coarse mesh results, fine mesh does improve the simulation results for all the RANS models at some wind attack angles. The largest deviation from experimental data for the *k*-*ω*-SST model is at a wind attack angle of 150^o, which is around 30%. With the coarse mesh, the C_p difference has been predicted using DES-SST and the LES model with Smagorinksy option. Either model gives both mean and peak wind load. However, they do not demonstrate better prediction of mean wind load than the *k*-*ω*-SST model. LES gives relatively better prediction in C_p difference than the DES-SST model, but it requires more computing power.

After simulation of the flow past a cube and the canopy flow with different models, the *k*-*ω*-SST and DES-SST models have been selected to conduct simulation of the wind load on roof mounted solar panels. Wind load on one of 16 solar panels in the corner of the roof of a building is tracked. For the *k*-*ω*-SST model, three levels mesh fineness have been used, while the coarsest mesh is used for the DES-SST. Simulation results show that with the finest mesh, *k*-*ω*-SST can accurately predict the C_p difference on solar panels at all wind attack angles except near 330^o, while it gives a more accurate prediction for the wind deflector at all wind attack angles. In terms of drag coefficient and lift coefficient on the assembly, *k*-*ω*-SST gives more accurate prediction of drag than of lift. Compared with the *k*-*ω*-SST model, DES-SST gives a less accurate prediction of both drag coefficient and lift coefficient. The peak load prediction from DES-SST is good for drag but not so good for lift when compared with experimental data. Both the DES-SST model and experimental results show similar mean and peak wind load trends vs. wind attack angle, which indicates that the mean wind load has a close relation with the peak wind load.

Based on the close relationship of the mean and peak wind load, we use the *k*-*ω*-SST model to disclose the wind load change with three different configurations, increasing the lateral space from 0.125 inches to 2.5 inches (Case1), increasing the vertical space from 1 inch to 6 inches (Case 2), increasing the vertical space to the same height as a parapet (Case 3). The simulations for Case 1 show that there is no drag change for most wind attack angles except in the 360^o to 330^o range. However, it will significantly reduce the wind lift force between 360^o and 320^o. For Case 2, the drag dramatically increases for wind attack angles from 360^o to 300^o, while the lift force is greatly reduced at these wind attack angles. For case 3, the drag increases significantly at wind attack angles from 360^o to 300^o, while the lift force reduces for wind attack angles from 360^o to 270^o and increases for 240^o to 180^o wind attack angles.

6.2 Future Work

On the basis of the analysis provided in this thesis, it is recommended that the mesh near the walls and solar panel surfaces be refined to better predict the wind load using the k-ω-SST, DES-SST and LES models. Tracking more solar panels near the roof corner will give more information about wind load on solar panels. Finally, carefully conducted experiments are warranted to provide more detailed data which can be used to validate the CFD models.

APPENDIX A

Turbulence Models

A.1 Reynolds Averaged Navier-Stokes (RANS) Models

In this Appendix, for simplicity, terms representing the effects of buoyancy, high Mach number and general source terms are not included in these RANS models.

In all RANS models the Reynolds stresses are computed from

$$\tau_{ij} = -\rho\overline{u_i'u_j'} = \mu_t\left(\frac{\partial U_i}{\partial x_j}+\frac{\partial U_j}{\partial x_i}\right) - \frac{2}{3}\rho k\delta_{ij} \qquad \text{(A-1)}$$

where δ_{ij} is the Kronecker delta,

$$\delta_{ij} = \begin{cases} 0 & if\ i \neq j \\ 1 & if\ i = j \end{cases}.$$

A.1.1 One-equation Model

a) Spalart-Allmaras [32]

Governing equation for the kinematic eddy viscosity parameter $(\tilde{v})$:

$$\frac{\partial(\rho\tilde{v})}{\partial t} + \frac{\partial(\rho\tilde{v}u_i)}{\partial x_i} = \frac{1}{\sigma_{\tilde{v}}}\frac{\partial}{\partial x_i}\left[(\mu+\rho\tilde{v})\frac{\partial\tilde{v}}{\partial x_i} + C_{b2}\rho\frac{\partial\tilde{v}}{\partial x_j}\frac{\partial\tilde{v}}{\partial x_j}\right] + C_{b1}\rho\tilde{v}\tilde{\Omega} - C_{w1}\rho\left(\frac{\tilde{v}}{y}\right)^2 f_w \qquad \text{(A-2)}$$

where

$\tilde{\Omega} = \Omega + \frac{\tilde{v}}{(\kappa y)^2}f_{v2}$ [turbulence production term]

y is distance from the wall, κ is von Karman's constant, and

$\Omega = \sqrt{2\Omega_{ij}\Omega_{ij}}$ [magnitude of vorticity]

$\Omega_{ij} = \frac{1}{2}\left(\frac{\partial U_i}{\partial x_j} - \frac{\partial U_j}{\partial x_i}\right)$ [rate-of-rotation tensor]

$f_{v2} = f_{v2}\left(\frac{\tilde{v}}{v}\right),\ f_w = f_w(\tilde{v}/(\tilde{\Omega}\kappa^2 y^2))$ [wall-damping functions]

$$C_{w1} = \frac{C_{b1}}{k^2} + \frac{1 + C_{b2}}{\sigma_{\tilde{v}}}$$

$\mu_t = \rho \tilde{v} f_{v1}$ [turbulent viscosity]

$f_{v1} = \frac{\chi^3}{\chi^3 + C_{v1}^3}$ [viscosity damping term]

$$\chi = \frac{\tilde{v}}{v}$$

Model constants are: $\sigma_{\tilde{v}} = \frac{2}{3},\ \kappa = 0.4187,\ C_{b1} = 0.1355,\ C_{b2} = 0.622,\ C_{v1} = 7.1.$

Since turbulent kinetic energy is not calculated in this model, the last term in equation (A-1) is ignored when calculating the Reynolds stresses.

A.1.2 Two-equation Models

a) *k*-*ε* standard

Governing equations for turbulent kinetic energy (*k*) and dissipation rate (*ε*):

$$\frac{\partial(\rho k)}{\partial t} + \frac{\partial(\rho k u_i)}{\partial x_i} = \frac{\partial}{\partial x_i}\left[(\mu + \frac{\mu_t}{\sigma_k})\frac{\partial k}{\partial x_i}\right] + G_k - Y_k \tag{A-3}$$

$$\frac{\partial(\rho \varepsilon)}{\partial t} + \frac{\partial(\rho \varepsilon u_i)}{\partial x_i} = \frac{\partial}{\partial x_i}\left[(\mu + \frac{\mu_t}{\sigma_\varepsilon})\frac{\partial \varepsilon}{\partial x_i}\right] + G_\varepsilon - Y_\varepsilon \tag{A-4}$$

where

$G_k = \mu_t S^2$ [kinetic energy production term]

$G_\varepsilon = C_{1\varepsilon}\frac{\varepsilon}{k}G_k$ [kinetic energy dissipation production term]

$S = \sqrt{2S_{ij}S_{ij}}$ [modulus of strain rate tensor]

$S_{ij} = \frac{1}{2}(\frac{\partial u_i}{\partial x_j} + \frac{\partial u_j}{\partial x_i})$ [strain rate tensor]

$Y_k = \rho\varepsilon$ [kinetic energy destruction term]

$Y_\varepsilon = C_{2\varepsilon}\frac{\varepsilon^2}{k}$ [dissipation rate destruction term]

$\mu_t = \rho C_\mu \frac{k^2}{\varepsilon}$ [turbulent viscosity]

Model constants are: $C_\mu = 0.09,\ \sigma_k = 1,\ \sigma_\varepsilon = 1.3,\ C_{1\varepsilon} = 1.44,\ C_{2\varepsilon} = 1.92.$

b) *k*-*ε* RNG

Governing equations for turbulent kinetic energy (*k*) and dissipation rate (*ε*):

$$\frac{\partial(\rho k)}{\partial t} + \frac{\partial(\rho k u_i)}{\partial x_i} = \frac{\partial}{\partial x_j}\left[\alpha_k \mu_{eff}\frac{\partial k}{\partial x_j}\right] + G_k - \rho\varepsilon \qquad \text{(A-5)}$$

$$\frac{\partial(\rho\varepsilon)}{\partial t} + \frac{\partial(\rho\varepsilon u_i)}{\partial x_i} = \frac{\partial}{\partial x_j}\left[\alpha_\varepsilon \mu_{eff}\frac{\partial \varepsilon}{\partial x_j}\right] + C_{1\varepsilon}\frac{\varepsilon}{k}G_k - C_{2\varepsilon}^*\rho\frac{\varepsilon^2}{k} \qquad \text{(A-6)}$$

where

$\mu_{eff} = \mu + \mu_t$. [effective viscosity]

The turbulent kinetic energy production term G_k is the same as in equation (A-3).

For constant $C_{2\varepsilon}^*$, the scale elimination procedure following RNG theory is used

$$C_{2\varepsilon}^* = C_{2\varepsilon} + \frac{C_\mu \eta^3\left(1-\frac{\eta}{\eta_0}\right)}{1+\beta\eta^3} \quad \text{where} \quad \eta = \frac{k}{\varepsilon}\sqrt{2S_{ij}.S_{ij}} \ .$$

Model constants are: $C_\mu = 0.0845,\ C_{1\varepsilon} = 1.42,\ C_{2\varepsilon} = 1.68,\ \eta_0 = 4.377,\ \beta = 0.012,$

and

$\alpha_k = \alpha_\varepsilon = 1.39,$ for high Re flow.

c) *k*-*ε* Realizable

Governing equation for turbulent dissipation rate (*ε*):

$$\frac{\partial(\rho\varepsilon)}{\partial t}+\frac{\partial(\rho\varepsilon u_j)}{\partial x_j}=\frac{\partial}{\partial x_j}\left[\left(\mu+\frac{\mu_t}{\sigma_\varepsilon}\right)\frac{\partial\varepsilon}{\partial x_j}\right]+\rho C_1 S\varepsilon-\rho C_2\frac{\varepsilon^2}{k+\sqrt{\nu\varepsilon}} \tag{A-7}$$

where S is modulus of the strain rate tensor defined in the *k*-*ε* standard model. The turbulent kinetic energy transport equation is the same as equation (A-3), except that the model constants have changed.

The turbulent viscosity is calculated following the same procedure as the *k*-*ε* standard model, but C_μ is a variable instead of a constant,

$$C_\mu=\frac{1}{A_0+A_s\frac{kU^*}{\varepsilon}} \qquad \text{where} \qquad U^*=\sqrt{S_{ij}S_{ij}+\tilde{\Omega}_{ij}\tilde{\Omega}_{ij}}$$

and $\tilde{\Omega}_{ij}=\Omega_{ij}-2\varepsilon_{ijk}\omega_k$, $\Omega_{ij}=\overline{\Omega}_{ij}-\varepsilon_{ijk}\omega_k$,

where $\overline{\Omega}_{ij}$ is the mean rate-of-rotation tensor viewed in a moving reference frame with the angular velocity of ω_k and ε_{ijk} is the permutation tensor. In these equations,

$$A_o=4.04,\ C_1=\max\left[0.43,\frac{\eta}{\eta+5}\right],\ \ \eta=S\frac{k}{\varepsilon}\sigma_\varepsilon,\ A_s=\sqrt{6}cos\phi$$

where $\phi=\frac{1}{3}\cos^{-1}(\sqrt{6}\,W)$, $W=\frac{S_{ij}S_{jk}S_{ki}}{\tilde{S}^3}$, $\tilde{S}=\sqrt{S_{ij}S_{ij}}$, S_{ij} is strain rate tensor.

Model constants are: $C_{1\varepsilon}=1.44$, $C_2=1.9$, $\sigma_k=1.0$, $\sigma_\varepsilon=1.2$.

d) *k*-*ω* standard

Governing equations for turbulent kinetic energy (*k*) and specific dissipation rate (*ω*):

$$\frac{\partial(\rho k)}{\partial t}+\frac{\partial(\rho k u_i)}{\partial x_i}=\frac{\partial}{\partial x_j}\left[\Gamma_k\frac{\partial k}{\partial x_j}\right]+\ G_k-Y_k \tag{A-8}$$

$$\frac{\partial(\rho\omega)}{\partial t}+\frac{\partial(\rho\omega u_i)}{\partial x_i}=\frac{\partial}{\partial x_j}\left[\Gamma_\omega\frac{\partial\omega}{\partial x_j}\right]+\ G_\omega-Y_\omega \tag{A-9}$$

where G_k and Y_k are kinetic energy production and destruction terms, respectively.

and G_k is identical to that of governing equations of k-ε and its variants

$$\Gamma_k = \mu + \frac{\mu_t}{\sigma_k} \ , \qquad \Gamma_\omega = \mu + \frac{\mu_t}{\sigma_\omega}$$

$\mu_t = \alpha^* \frac{\rho k}{\omega}$ [turbulent viscosity for a low Re]

$$\alpha^* = \alpha^*_\infty \left(\frac{\alpha^*_0 + \frac{Re_t}{R_k}}{1 + \frac{Re_t}{R_k}} \right)$$

$Re_t = \frac{\rho k}{\mu \omega}, \ R_k = 6.0, \ \alpha^*_0 = \frac{\beta_i}{3}, \ \beta_i = 0.072.$

At high Reynolds number, $\alpha^*$and α^*_∞ are both taken to be 1.

$G_\omega = \alpha \frac{\omega}{k} G_k$ [specific dissipation rate production term]

$$\alpha = \frac{\alpha_\infty}{\alpha^*} \left(\frac{\alpha_0 + \frac{Re_t}{R_\omega}}{1 + \frac{Re_t}{R_\omega}} \right)$$

where $R_\omega = 2.95$, α* and Re_t are defined as above.

For high Re, α and α_∞ are both taken to be 1.

$Y_k = \rho \beta^* f_{\beta^*} k \omega$ [kinetic energy destruction term]

where $f_{\beta^*} = \frac{1+680x_k^2}{1+400x_k^2}$ with

$$x_k = \begin{cases} 1 & if \ x_k > 0 \\ \dfrac{1}{\omega^3} \dfrac{\partial k}{\partial x_j} \dfrac{\partial \omega}{\partial x_j} & if x_k \leq 0 \end{cases},$$

$\beta^* = \beta^*_i [1 + \zeta^* F(M_t)]$, where $\zeta^* = 1.5$ and $F(M_t) = 0$ when in low Mach number flow, and

$$\beta_i^* = \beta_\infty^* \left(\frac{\frac{4}{15} + \left(\frac{Re_t}{R_\beta}\right)^4}{1 + \left(\frac{Re_t}{R_\beta}\right)^4} \right)$$

where $R_\beta = 8.0,\ \beta_\infty^* = 0.09$ and Re_t is calculated as above.

$Y_\omega = \rho\beta f_\beta \omega^2$ [specific dissipation rate destruction term]

where β is related to fluid Mach number, when in low Mach number, $\beta = \beta_i$

$$f_\beta = \frac{1 + 70x_\omega}{1 + 80x_\omega}$$

$$x_\omega = \left| \frac{\Omega_{ij}\Omega_{jk}S_{ki}}{(\beta_\infty^*\omega)^3} \right|$$

where S_{ki} and Ω_{ij} are the strain rate tensor and rotation rate tensor, respectively. They are calculated the same way as in the Spalart-Allmaras model and *k*-*ε* standard model.

For incompressible flow and high Re,

$\beta^* = \beta_i^*,\ \beta_i^* = \beta_\infty^*$.

Model constants are: $\sigma_k = 2.0,\ \sigma_\omega = 2.0,\ \alpha_\infty^* = 1,\ \alpha_\infty = 0.52,\ \alpha_0 = \frac{1}{9},\ \beta_\infty^* = 0.09,$ $\beta_i = 0.072,\ R_\beta = 8.0,\ R_k = 6.0,\ R_\omega = 2.95,\ M_{to} = 0.25.$

e) *k*-*ω*-SST

Governing equations for turbulent kinetic energy (*k*) and specific dissipation rate (*ω*):

$$\frac{\partial(\rho k)}{\partial t} + \frac{\partial(\rho k u_i)}{\partial x_i} = \frac{\partial}{\partial x_j}\left[\Gamma_k \frac{\partial k}{\partial x_j}\right] + \tilde{G}_k - Y_k \qquad \text{(A-10)}$$

$$\frac{\partial(\rho\omega)}{\partial t} + \frac{\partial(\rho k u_i)}{\partial x_i} = \frac{\partial}{\partial x_j}\left[\Gamma_\omega \frac{\partial k}{\partial x_j}\right] + G_\omega - Y_\omega + D_\omega \qquad \text{(A-11)}$$

Both diffusion coefficients Γ_k and Γ_ω have the same form of those in *k*-*ω* standard model, but the turbulent viscosity is computed from

$$\mu_t = \frac{\rho k}{\omega} \frac{1}{max\left[\frac{1}{a^*}, \frac{SF_2}{a_1 \omega}\right]} ,$$

where *S* is modulus of the strain rate tensor, and

$$\sigma_k = \frac{1}{\frac{F_1}{\sigma_{k,1}} + \frac{(1-F_1)}{\sigma_{k,2}}}$$ [Prandtl number]

$$\sigma_\omega = \frac{1}{\frac{F_1}{\sigma_{\omega,1}} + \frac{(1-F_1)}{\sigma_{\omega,2}}}$$ [Prandtl number]

a^* is a damping factor which is the same as in the *k*-*ω* standard model, and F_1 , F_2 are blending functions.

$$G_\omega = \frac{\alpha}{\nu_t} \tilde{G}_k,$$ [production of specific dissipation rate]

$$\tilde{G}_k = \min(G_k, 10\rho\beta^* k\omega)$$ [production of kinetic energy]

α takes the same form as in the *k*-*ω* standard model, however α_∞ in that model is constant, while here it is variable, given by

$$\alpha_\infty = F_1 \alpha_{\infty,1} + (1 - F_1)\alpha_{\infty,2}$$

where $\alpha_{\infty,1} = \frac{\beta_{i,1}}{\beta^*_\infty} - \frac{\kappa 1^2}{\sigma_{\omega,1}\sqrt{\beta^*_\infty}}$, $\alpha_{\infty,2} = \frac{\beta_{i,2}}{\beta^*_\infty} - \frac{\kappa 1^2}{\sigma_{\omega,2}\sqrt{\beta^*_\infty}}$, and $\kappa 1 = 0.41$.

In equations (A-10) and (A-11), the dissipation terms are defined as

$$Y_k = \rho\beta^* k\omega$$ [dissipation of *k*]

where β^* is the same as in the *k*-*ω* standard model, and

$$Y_\omega = \rho\beta\omega^2$$ [dissipation of *ω*]

where β is the same as in the *k*-*ω* standard model, in the equation of β, β_i is obtained from

$$\beta_i = F_1\beta_{i,1} + (1 - F_1)\beta_{i,2}$$

$D_\omega = 2(1 - F_1)\rho \frac{1}{\omega\sigma_{\omega,2}}\frac{\partial k}{\partial x_j}\frac{\partial \omega}{\partial x_j}$, [cross-diffusion modification]

Model constants are: $\sigma_k = 1.0,\ \sigma_{\omega,1} = 2.0,\ \sigma_{\omega,2} = 1.17,\ \beta^* = 0.09,\ \beta_{i,1} = 0.075,$ $\beta_{i,2} = 0.0828.$

A.1.3 Reynolds Stress Model

Governing equations for the Reynolds stresses $\overline{u_i'u_j'}$ (*i*,*j* = 1,2,3) are:

$$\frac{\partial}{\partial t}(\rho\overline{u_i'u_j'}) + C_{ij} = P_{ij} + D_{ij} - \varepsilon_{ij} + \Phi_{ij} + \Omega_{ij} \qquad \text{(A-12)}$$

In these equations,

$C_{ij} = \frac{\partial}{\partial x_k}(\rho u_k\overline{u_i'u_j'})$ [convection term of Reynolds stress transport]

$P_{ij} = -\rho(\overline{u_i'u_k'}\frac{\partial U_j}{\partial x_k} + \overline{u_j'u_k'}\frac{\partial U_i}{\partial x_k})$ [production term of Reynolds stress transport]

$\Omega_{ij} = -2\rho\Omega_k(\overline{u_j'u_m'}e_{ikm} + \overline{u_i'u_m'}e_{jkm})$, [rotation term of Reynolds stress transport]

where ω_k is the rotation vector; e_{ijk} equals 1 if *i*, *j*, *k* are different and in cyclic order, equals -1 if indices are in anti-cyclic order, and equals zero if two indices are the same.

$D_{ij} = \frac{\partial}{\partial x_k}(\frac{\mu_t}{\sigma_k}\frac{\partial\overline{u_i'u_j'}}{\partial x_k})$ [diffusion term of Reynolds stress transport]

where $\sigma_k = 0.82$ and

$\mu_t = \rho C_\mu\frac{k^2}{\varepsilon}$, with $C_\mu = 0.09$, and

$\varepsilon_{ij} = \frac{2}{3}\varepsilon\delta_{ij}$ [dissipation term of Reynolds stress transport]

where δ_{ij} is the Kronecker delta.

$\Phi_{ij} = \overline{p\left(\frac{\partial u_\imath'}{\partial x_\jmath} + \frac{\partial u_\jmath'}{\partial x_\imath}\right)}$ [pressure strain term of Reynolds stress transport]

In the classic approach, the pressure strain term is decomposed into three components

$$\phi_{ij} = \phi_{ij,1} + \phi_{ij,2} + \phi_{ij,w}$$

where

$\phi_{ij,1} = -C_1 \rho \frac{\varepsilon}{k}\left[\overline{u_\imath' u_\jmath'} - \frac{2}{3}\delta_{ij} k\right]$ [slow pressure-strain term]

$$\phi_{ij,2} = -C_2[\left(P_{ij} + F_{ij} + 5G_{ij}/6 - C_{ij}\right) - \frac{1}{3}\delta_{ij}(P_{kk} + 5G_{kk}/6 - C_{kk})]$$

[rapid pressure-strain term]

$$\phi_{ij,w} = C_1' \frac{\varepsilon}{k}\left(\overline{u_k' u_m'} n_k n_m \delta_{ij} - \frac{3}{2}\overline{u_\imath' u_k'} n_j n_k - \frac{3}{2}\overline{u_\jmath' u_k'} n_i n_k\right)\frac{C_l k^{\frac{3}{2}}}{\varepsilon d}$$

$$+C_2^1(\phi_{km,2} n_k n_m \delta_{ij} - \frac{3}{2}\phi_{ik,2} n_j n_k - \frac{3}{2}\phi_{jk,2} n_i n_k)\frac{C_l k^{\frac{3}{2}}}{\varepsilon d}$$ [wall reflection term]

where $C_1 = 1.8,\ C_2 = 0.6,\ C_1' = 0.5,\ C_2' = 0.3$, and

n_k is the x_k component of the unit normal to the wall, *d* is the distance to the wall, and $C_l = \frac{C_\mu^{3/4}}{\kappa}$, with κ = 0.4187 and C_μ = 0.09.

The scalar dissipation rate *ε* is modeled similar with the *k*-*ε* standard model.

A.2 Large Eddy Simulation (LES)

Based on the Boussinesq hypothesis, the subgrid stresses are calculated from:

$$\tau_{ij} = -2\mu_{SGS}\bar{S}_{ij} + \frac{1}{3}\tau_{kk}\delta_{ij} \qquad \text{(A-13)}$$

where $\mu_{SGS} = \rho {L_s}^2 \sqrt{2\bar{S}_{ij}\bar{S}_{ij}}$, [subgrid viscosity]

$\bar{S}_{ij} = \frac{1}{2}(\frac{\partial \bar{u}_i}{\partial x_j} + \frac{\partial \bar{u}_j}{\partial x_i})$, [strain rate tensor for resolved scale]

$L_s = \min(\kappa d, C_s \Delta)$ [mixing length for subgrid scales]

κ is the von Karman constant, d is distance to the closest wall and C_s is the Smagorinsky constant, which is not a universal constant.

$\Delta = V^{1/3}$ [local grid scale]

where V is computational cell volume.

In equation (A-13), the τ_{kk} subgrid-scale stresses are not modeled. For incompressible flow, terms involving τ_{kk} can be added to the filtered pressure or simply neglected.

The dynamic subgrid-scale (SGS) model proposed by Germano et al. [7] determines the SGS stress difference with two different filtering operations with cutoff widths Δ_1 and Δ_2,

$$\tau_{ij}^{(2)} - \tau_{ij}^{(1)} = \rho \overline{\bar{u}_i \bar{u}_j} - \rho \bar{\bar{u}}_i \bar{\bar{u}}_j \tag{A-14}$$

where the bracketed superscripts (1) and (2) indicating filtering at cutoff widths Δ_1 and Δ_2, respectively.

In the case of bluff body flows, Germano's SGS model usually gives better simulation results [22]. This option is used in the current research.

Large Eddy Simulation (LES) needs much more computing power than RANS models, but it gives more accurate results in the case of bluff body flows.

A.3 Detached Eddy Simulation (DES)

In the Detached Eddy Simulation (DES) approach, the unsteady RANS models are employed in the boundary layer and LES is applied in the separated regions. DES models have been specially designed to address high Reynolds number wall bounded flows, where the cost of computation is very high when using LES. The computational cost for DES is lower than LES but is higher than RANS. Fluent offers three types of RANS model for DES, the Spalart-Allmaras model, the k-ε Realizable model and the k-ω-SST model.

In the current research, the k-ω-SST based DES proposed by Menter et al. [20], has been used.

The kinetic energy dissipation term in the transport equation is imbedded into the DES model through the following formula:

$$Y_k = \rho\beta^* k\omega F_{DES}$$

where $F_{DES} = \max(\frac{L_t}{C_{des}\Delta_{max}}, 1)$, $C_{des} = 0.61$, Δ_{max} is maximum of the local grid spacing Δ_x, Δ_y, Δ_z and

$L_t = \frac{\sqrt{k}}{\beta^*\omega}$ [turbulent length scale]

which is used to define the RANS model, where k is turbulent kinetic energy, ω is specific dissipation rate and β^* = 0.09 for high Reynolds number incompressible flow.

APPENDIX B

Near-Wall Treatment

The presence of a wall not only greatly changes the mean flow to satisfy the no-slip condition, but also dramatically influences the turbulent characteristics near the wall. Near the wall, the mean velocity experiences a large gradient, and the fluctuations of the flow in all three directions reduce from their peak value to zero at the wall surface due to the damping effect of the wall. Among the three components, the streamwise fluctuation has the highest peak value near the wall.

Numerous experiments demonstrate that the near-wall flow region can be subdivided into three layers; the viscous layer, the buffer layer and the outer layer. Inside the viscous layer, also called the laminar layer, the viscous force plays the dominant role. In the outer layer, the turbulent Reynolds stresses have a major role, while in the buffer layer, both viscous and turbulence forces share an equal role.

Traditionally, there are two approaches to model the near-wall flow region. One approach is to use the "standard wall function", which uses an empirical equation to "bridge" the viscous layer to the outer layer, and the viscous region is not resolved [3]. This approach saves computing cost, but the accuracy of the solution gets worse once the y* value reaches 15, when the mesh near the wall gets refined. Another approach is to use a wall model near the wall [3], so the flow inside the three layers all get resolved. The mesh near the viscous layer is usually very fine in this case.

B.1 Standard Wall Function

The law-of-the-wall for mean velocity is

$$U^* = \frac{1}{\kappa}\ln(Ey^*) \tag{B-1}$$

where $U^* = \frac{U_p C_\mu^{1/4} k_p^{1/2}}{\tau_w/\rho}$

and $y^* = \frac{\rho C_\mu^{1/4} k_p^{1/2} y_p}{\mu}$.

Here κ is the von Karman constant, equal to 0.4187, E = 0.793, U_p is the mean velocity at the near wall node P, k_p is turbulent kinetic energy at node P, y_p is the distance from the wall to the node P and μ is the dynamic viscosity of the fluid. The $y*$ value should be of the order of 15 at the low end, and the high end value depends on the Reynolds number of the flow.

In Fluent, once $y* > 11$, the log-law is employed. When $y* < 11$, the laminar strain-stress relationship is used,

$U* = y*$.

B.2 Scalable Wall Functions

In Fluent, a scalable wall function has been introduced to avoid solution deterioration when $y* < 11$ for a refined mesh. For $y* > 11$, the scalable wall function is identical to the standard wall function. When $y* < 11$, a limiter is introduced,

$\tilde{y}^* = \max(y^*, y^*_{limit})$, where $y^*_{limit} = 11$.

B.3 Enhanced Wall Treatment

Fluent combines the two-layer model with the so-called "enhanced wall function", in order to reach the goal of obtaining the accuracy of the two-layer model when $y^+ \approx 1$, and not significantly reducing the accuracy of the standard wall function meshes. In this approach, the whole computation domain is subdivided into a viscosity-affected region and a fully-turbulent region. The demarcation of the two regions is determined by a wall distance-based turbulent Reynolds number, Re_y, which is defined as

$$Re_y = \frac{\rho y \sqrt{k}}{\mu},$$

where y is the normal distance from the wall.

When $Re_y > Re_y^*$, where Re_y^* = 200, the *k*-*ε* or RSM is activated, when $Re_y < Re_y^*$, the one-equation model of Wolfstein [3] is activated.

The law-of-the-wall has been modified as a single wall law for the entire wall region,

$$u^+ = e^{\Gamma} u_{lam}^+ + e^{\frac{1}{\Gamma}} u_{turb}^+ \, , \tag{B-2}$$

where the blending function $\Gamma = -\frac{a(y^+)^4}{1+by^+}$

and *a* = 0.01, *b* = 5.

$$\frac{du^+}{dy^+} = e^{\Gamma} \frac{du_{lam}^+}{dy^+} + e^{\frac{1}{\Gamma}} \frac{du_{turb}^+}{dy^+}$$

B.4 LES Near-Wall Treatment

When the mesh is fine enough to resolve the laminar sublayer, the wall shear stress is obtained from the laminar stress-strain relationship,

$$\frac{\bar{u}}{u_\tau} = \frac{\rho u_\tau y}{\mu} \, .$$

If the mesh is very coarse, then the law-of-the-wall is applied,

$$\frac{\bar{u}}{u_\tau} = \frac{1}{\kappa} lnE(\frac{\rho u_\tau}{\mu}).$$

If the first near-wall point lies in the buffer region, equation (B-2) can be used.

Another approach is to use the Werner and Wengle wall function [36]. When the cells at the wall are not very fine, the following wall function can give better simulation results than the two-layer wall model [3],

$$|\tau_w| = \frac{2\mu|u_p|}{\Delta z} \, , \quad \text{for} \quad |u_p| \leq \frac{\mu}{2\rho\Delta z} A^{\frac{2}{1-B}} \tag{B-3}$$

$$|\tau_w| = \rho \left[\frac{1-B}{2} A^{\frac{1+B}{1-B}} (\frac{\mu}{\rho\Delta z})^{1+B} + \frac{1+B}{A} (\frac{\mu}{\rho\Delta z})^{B} |u_p| \right]^{\frac{2}{1+B}}, \quad \text{for} \quad |u_p| \geq \frac{\mu}{2\rho\Delta z} A^{\frac{2}{1-B}}$$

REFERENCES

[1] Adrian, R., Steady Wind Pressures on Solar Collectors on Flat-Roofed Buildings. *J. of Wind Eng. and Ind. Aerodyn.*, Vol. 23(1), pp. 249-258, 1985.

[2] Adrian, R., Wind Forces on Structures Supporting Solar Collectors. *J. of Wind Eng. and Ind. Aerodyn.*, Vol. 32(1), pp. 93-100, 1989.

[3] *ANSYS Theory Guide, Release 13.0*, pp. 121-122, 2010.

[4] ASCE 7-05 *Minimum Design Loads for Buildings and Other Structures*, American Society of Civel Engineers, Jan, 2006, ISBN: 0784408092.

[5] Bronkhorst, A., Franke, J., Geurts, C., Bentum, C.V. and Grepinet, F., Wind Tunnel and CFD Modelling of Wind Pressures on Solar Energy Systems on Flat Roofs. *The Fifth International Symposium on Computational Wind Engineering (CWE2010),* Chapel Hill, North Carolina, USA, May 23-27, 2010.

[6] Franke, J., Hellsten, A., Schlünzen, H. and Carissimo, B., Best Practice Guideline for the CFD Simulation of Flows in the Urban Environment. *COST Action 732*, 2007.

[7] Germano, M., Piomelli, U., Moin, P. and Cabot, W.H., A Dynamic Subgrid Scale Eddy Viscosity Model. *Phys. Fluids A*, Vol. 3, pp. 1760-1765, 1991.

[8] Ginger, G.D. and Letchford, C.W., Wind Load on Canopy Roofs. *Research Report Series,* University of Queensland, Department of Civil Engineering, Vol. 132, pp. 1-74, 1991.

[9] Graeme, W., Wind Loads on Industrial Solar Panel Arrays and Supporting Roof Structure. *Wind and Structures,* Vol. 4(6), pp. 481-494, 2001.

[10] Haupt, S.E., Zajaczkowski, F.J. and Peltier, L.J., Detached Eddy Simulation of Atmospheric Flow about a Surface Mounted Cube at High Reynolds Number. *J. of Fluids Eng.,*Vol. 133(3), 031002, 2011.

[11] Holmes, D.J., *Wind Loading of Structures.* Spon Press, London, 2001.

[12] Köse, D.A. and Dick, E., Prediction of the Pressure Distribution on a Cubical Building with Implicit LES. *J. of Wind Eng. and Ind. Aerodyn.*, Vol. 98, pp. 628-649, 2010.

[13] Launder, B.E., Reece, G.J. and Rodi, W., Progress in the Development of a Reynolds-Stress Turbulence Closure. *J. of Fluid Mech*., Vol. 68(3), pp. 537-566, 1975.

[14] Launder, B.E. and Spalding, D.B., The Numerical Computation of Turbulent Flows. *Comput. Methods in Appl. Mech. Eng*., Vol. 3, pp. 269-289, 1974.

[15] Lilly, D.K., On the Application of the Eddy Viscosity Concept in the Inertial Sub-range of Turbulence. *NCAR Report No. 123*, 1966.

[16] Limon, S., Computation of Internal Separated Flows Using a Zonal Detached Eddy Simulation Approach, *Proceedings of IMECE 03*, Paper No. IMECE 2003-43881, 2003.

[17] Lund, T.S., Wu, X. and Squires, K.D., Generation of Turbulent Inflow Data for Spatially Developing Boundary Layer Simulations. *J. of Comput. Phys.*, Vol. 140, pp. 233-258, 1998.

[18] Martinuzzi, R. and Tropea, C., The Flow around Surface-Mounted Prismatic Obstacles Placed in a Fully Developed Flow. *J. of Fluids Eng.*, Vol. 115, pp. 85-92, 1993.

[19] Mathey, F., Cokljat, D., Bertoglio, J.P., and Sergent, E., Specification of LES inlet boundary condition using vortex method. In Hanjali, K., Nagano, Y., and Tummers, M., editors 4th Internaltional Symposium on Turbulence, Heat and Mass Transfer, Antalya, Turkey. Begell House, Inc. 2003.

[20] Menter, F.R., Performance of Popular Turbulence Models for Attached and Separated Adverse Pressure Gradient Flow. *AIAA J.*, Vol. 30, pp. 2066-2072, 1992.

[21] Menter, F.R., Kuntz, M. and Langtry, R., Ten Years of Experience with the SST Turbulence Model. In Hanjalic, K., Nagano, Y. and Tummers, M., Editors *Turbulence, Heat and Mass Transfer*, 4, Begell House Inc., pp. 625-632, 2003.

[22] Murakami, S., Overview of Turbulence Models Applied in CWE-1997. *2nd European & African Conference on Wind Engineering*, Genova, Italy, 1997.

[23] Nozawa, K. and Tamura, T., Large Eddy Simulation of the Flow around a Low-Rise Building Immersed in a Rough-Wall Turbulent Boundary Layer. *J. of Wind Eng. and Ind. Aerodyn.*, Vol. 90, pp. 1151-1162, 2002.

[24] Patankar, S.V., and Spalding, D. B., A Calculation Procedure for Heat, Mass and Momentum Transfer in Three-dimensional Parabolic Flows, Int. J. Heat Mass Transfer, 15:1787-1806,1972.

[25] Richards, P., A 6m Cube in an Atmospheric Boundary Layer Flow, Part 2, Computational Solutions. *Wind and Structures*, Vol. 5(2-4), pp. 177-192, 2002.

[26] Rodi, W., Experience with Two-Layer Models Combining the k-ε Models with a One-equation Model near the Wall. *AIAA Paper* 91-0216, 1991.

[27] Rodi, W., Large-eddy Simulation of the Flow past Bluff Bodies: State-of-the-Art. *JSME International Journal*, *Series B*, *Fluids and Thermal Eng.*, Vol. 41(2), pp. 361-374, 1998.

[28] RWDI, Design Wind Pressure Study, Project #1010475, Apr. 2010.

[29] Shah, K.B. and Ferziger, J.H., A Fluid Mechanicians View of Wind Engineering: Large Eddy Simulation of Flow past a Cubic Obstacle. *J. of Wind Eng. and Ind*. *Aerodyn.,* Vol. 67-68, pp. 211-224, 1997.

[30] Shih, T.H., Liou, W.W., Shabbir, A., Yang, Z. and Zhou, J., A New k-ε Eddy-Viscosity Model for High Reynolds Number Turbulent Flows- Model Development and Validation. *Computers & Fluids*, Vol. 24(3), pp. 227-238, 1995.

[31] Shuzo, M., 3-D Numerical Simulation of Air Flow around a Cubic Model by Means of the k-ε Model. *J. of Wind Eng. and Ind. Aerodyn.*, Vol. 31(2), pp. 283-303, 1988.

[32] Spalart, P.R. and Allmaras, S.A., One-equation Turbulence Model for Aerodynamic Flows. *AIAA Paper* 92-0439, 1992.

[33] Spalart, P.R., Jou, W.H., Strelets, M. and Allmaras, S.A., Comments on the Feasibility of LES for Winds and on a Hybrid RANS/LES Approach. *First AFOSR International Conference on DNS/LES*, Ruston, LA, 1997.

[34] Tsuchiya, M., Murakami, S., Mochida, A., Kondo, K. and Ishida, Y., Development of a New *k*-*ε* Model for Flow and Pressure Fields around Bluff Body. *J. of Wind Eng. and Ind. Aerodyn*., Vol. 67-68, pp. 169-182, 1997.

[35] Versteeg, H.K. and Malalasekera, W., An Introduction to Computational Fluid Dynamics. Second Edition. *Pearson Prentice Hall*, 2007.

[36] Werner, H. and Wengle, H., Large-Eddy Simulation of Turbulent Flow over and around a Cube in a Plate Channel. In *Eighth Symposium on Turbulent Shear Flows*, Munich, Germany, 1991.

[37] Wilcox, D.C., Reassessment of the Scale-determining Equation for Advanced Turbulence Models. *AIAA J.*, Vol. 26(11), pp.1299-1310, 1988.

[38] Wolfshtein, M., The Velocity and Temperature Distribution of One-Dimensional Flow with Turbulence Augmentation and Pressure Gradient. *Int. J. of Heat Mass Transfer*, Vol. 12, pp. 301-318, 1969.

[39] Yakhot, V. and Orszag, S.A., Renormalization Group Analysis of Turbulence. *J. of Scientific Computing*, Vol. 1(1), pp. 3-51, 1986.

[40] Zhou, Y. and Zhang, Q., Numerical Simulation of Wind Pressure Distribution on Structure Roofs with Suspension Solar Panels. *Advanced Materials Research*, Vol. 163-167, pp. 3943-3946, 2011.

VITA AUCTORIS

Yuanming Yu was born in 1968 in Zhejiang, China. He received the BSc in Mechanical Engineering with specialization in shipbuilding process and its facilities from University of Wuhan, Water Transportation Engineering in 1990. He received the BASc in Mechanical Engineering with major in Automotive Engineering from University of Windsor, Ontario, in 2009. He currently is a candidate for the Master of Applied Science degree in Mechanical Engineering at University of Windsor with specialization in Thermo-Fluid Mechanics, and expects to graduate in May 2012.